ABSTRACT

Circuit Modeling and Optimization Techniques for Next-Generation Radar

Zachary Hays, M.S.E.C.E.

Mentor: Charles P. Baylis II, Ph.D.

Spectral emission requirements for radar systems are becoming increasingly strict. Future radar systems will require well-designed, reconfigurable circuitry to coexist with the myriads of other wireless devices using the spectrum. There are two main goals of this research. The first goal is to demonstrate circuit optimization algorithms implemented in real-time with two types of fast tuners. The optimization algorithms can tune the fundamental tuning elements of the tuner to quickly find an efficient operating point for the power amplifier while staying within spectral constraints. Secondly, this thesis presents a new method to model wideband low-noise amplifiers for use in receiver circuits using the Volterra Series. Both of these contributions are expected to enhance design and implementation of future radar systems.

Circuit Modeling and Optimization Techniques for Next-Generation Radar

by

Zachary Hays, B.S.E.C.E.

A Thesis

Approved by the Department of Electrical and Computer Engineering

_____

Kwang Y. Lee, Ph.D., Chairperson

Submitted to the Graduate Faculty of
Baylor University in Partial Fulfillment of the
Requirements for the Degree
of

Master of Science in Electrical and Computer Engineering

Approved by the Thesis Committee

_____

Charles P. Baylis, Ph.D., Chairperson

_____

Robert J. Marks II., Ph.D.

_____

Carolyn Skurla, Ph.D.

Accepted by the Graduate School

May 2018

_____

J. Larry Lyon, Ph.D., Dean

Page bearing signatures is kept on file in the Graduate School.

Copyright © 2018 by Zachary S. Hays

All rights reserved

TABLE OF CONTENTS

LIST OF FIGURES

LIST OF TABLES

ACKNOWLEDGMENTS

I would like to thank Dr. Charles Baylis for his mentoring and guidance as my graduate advisor and Dr. Robert Marks for his work and encouragement. I would like to thank my fellow graduate students, Austin Egbert, Casey Latham, Sarvin Rezayet, and previous graduate students, Matthew Fellows and Joseph Barkate, for all their input and comradery. I would especially like to thank my wife, Luci Hays, for her brilliant ideas in the research as well as being the entertainment chair of our research group. I would like to acknowledge Keysight Technologies for their donation of ADS, Modelithics for their donation of simulation model libraries, and Maury Microwave for their donation of SNP files for our bench equipment. I would like to thank Purdue University for their collaboration on the evanescent-mode cavity tuner. Finally, I would like to acknowledge John Clark, Ed Vivieros, and Steve Lardizabal for their helpful collaboration and guidance of this work.

ATTRIBUTIONS

The work presented in this thesis would not be possible without the ideas and work of the many coauthors on the papers contributing to this thesis. The contributions of each of the authors of [2, 3, 32] are described below.

In [2], two methods of tuning the varactor matching network were presented. The first method described in the paper is an impedance-based search algorithm in the Smith Chart. This search uses a lookup table between the bias voltages and impedances. This method was implemented on the bench by Luci Hays, and she is the first author on this paper. Walden and Rezayat helped take measurements for this method. The second method is a bias voltage search. Luci Hays proposed the idea of the interval halving search in the bias voltage space. I implemented this method onto the bench as well as the gradient search in the bias voltage space. Kappelmann and Egbert helped write code and take data for this method. Chapter Three contains the details of my contributions to this work. Baylis, Marks, Fellows, Penn, Viveiros, Hedden, Darwish provided guidance and advice for the work. Baylis proofread this work and helped author the paper.

In [32], the varactor matching network was first demonstrated for real-time PAE/ACPR optimization algorithms. The tuner was fabricated by Barlow and Flachsbart. The bench setup and calibration code was done by Kappelmann. Rezayat contributed to the code and measurements. I wrote the majority of the MATLAB code to run the search algorithm and took measurements and was first author on the paper.

Vivieros, Hedden, Penn, Marks, and Baylis provided helpful guidance to the project. Baylis contributed a large portion of the writing.

In [3], the interval halving algorithm first demonstrated in [2] is now demonstrated with the evanescent-mode cavity tuner. This tuner was designed and fabricated by Peroulis, Khater, and Semnani. I wrote the MATLAB code for the search algorithms and ran all the bench measurements for the interval halving search. Viveiros and Baylis guided the work. Baylis helped write and proofread the paper.

CHAPTER ONE

Introduction

The increasing demand on the frequency spectrum will require future radar systems to use the spectrum more efficiently and intelligently. The ever-growing number of wireless devices makes the need for spectrum sharing a priority for all devices, especially radar systems. The National Broadband Plan of 2010 requires the release of 500MHz of spectrum for wireless communications by 2020, and a significant part of the spectrum is expected to be taken from radar applications. These radar systems must maintain high performance while using a smaller bandwidth to stay within the stricter spectrum regulations.

One proposed solution to the crowded spectrum is the use of dynamic spectrum access with cognitive radar [1]. Instead of a fixed bandwidth and center frequency, a next-generation radar system would be able to detect nearby users in the spectrum and then reconfigure its circuitry to optimize performance at a frequency and bandwidth that will not interfere with those other users. This will require a fundamental change in the design and implementation of the radar's power amplifier and receiver. First, fast optimization algorithms will be required to quickly tune the matching network of the power amplifier to achieve high efficiency while ensuring no interference with neighboring systems. Second, better modeling techniques for design and simulation of the wide-band low power amplifiers will improve the linearity of the radar receiver and allow for higher resolution radar detection.

This thesis presents optimization algorithms implemented in simulation and measurement on two different output matching networks, as well a new technique to model wide-band low noise amplifiers using the Volterra Series. Chapter Two gives background information, which includes defining key terms and reviewing previous work in these areas. Chapter Three discusses search algorithms implemented with a varactor diode matching network and was originally published in [2]. Chapter Four shows these algorithms implemented with an evanescent-mode cavity tuner and published in [3]. Chapter Five explains how the Volterra Series can be used to improve in-band models for low noise amplifiers (LNAs). Chapter Six concludes the work by noting where this work contributes to the fields of circuit optimization and LNA design and simulation.

CHAPTER TWO

Background

This chapter discusses the background of the subject matter of this thesis and shows the state of the art in these topics. First, it is helpful to define terms used in the following chapters. Next, the concept of matching networks is explained for load pull and circuit optimization applications. The state-of-the-art of reconfigurable circuitry and matching networks is described in Section 2.1.3.

2.1 Definition of Key Concepts and Search Parameters

Reconfigurable matching networks can be tuned in real time to optimize several performance criteria. Two performance criteria which are discussed here in depth are power-added efficiency (PAE) and adjacent channel power ratio (ACPR). A power amplifier converts DC power to the RF power of the signal. PAE shows the efficiency of this power conversion, and it is defined by

$$PAE = \frac{P_{out,RF} - P_{in,RF}}{P_{DC}} \times 100\%. \tag{2.1}$$

A high PAE is an important design criterion, as much of the power lost in a radar transmitter is due to inefficiency of the power amplifier.

ACPR shows the ratio of power that spreads into the neighboring frequency bands to the power in the main operating frequency band as shown by (2.2).

$$ACPR = \frac{P_{RF,adj\ channels}}{P_{RF,main\ channel}} \tag{2.2}$$

The ACPR of an amplifier is ideally small, since power that is spread into the adjacent bands will interfere will users in those frequency bands [4], [5]. Power spreading is due to the nonlinearities in the power amplifier. However, operating a power amplifier nonlinearly will usually increase the PAE of the device, illustrating a tradeoff between PAE and ACPR performance. The search algorithms described in this thesis will find the optimal load impedance to the amplifier which will maximize PAE while staying within an ACPR constraint.

The Smith Chart is the two-dimensional graphical representation of the impedance plotted on the complex reflection coefficient plane and normalized to the characteristic impedance. The Smith Chart represents the relation

$$\Gamma = \frac{Z - Z_0}{Z + Z_0}$$

where Z_0 is the characteristic impedance which is 50Ω for all references in this thesis.

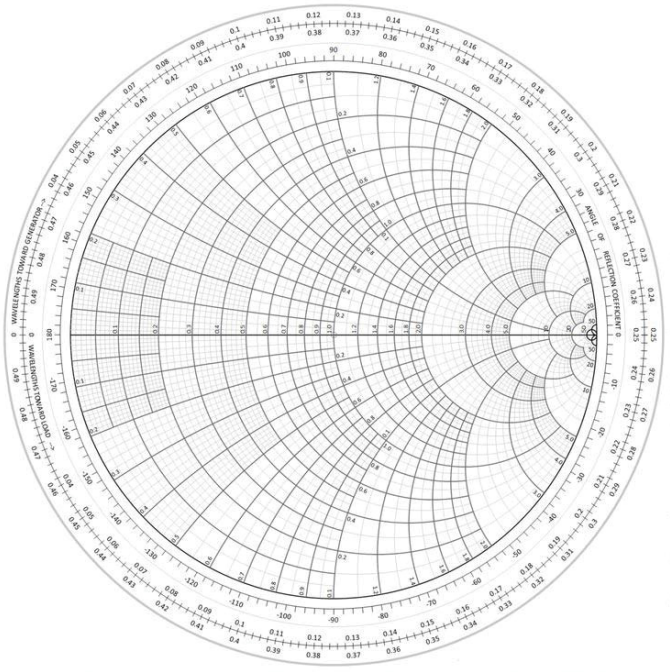

Figure 2.1: The Smith Chart

Figure 2.1 shows the Smith Chart. The Smith Chart is a tool to visualize the impedance and reflection coefficient, Γ, at the input or output of a device. The horizontal axis represents the real part of the complex impedance and the vertical axis represents the imaginary part of the impedance.

Both PAE and ACPR are functions of the load reflection coefficient, Γ_L. It is typical to show contour maps of PAE and ACPR on the Smith Chart as seen in Figure 2.2 below. Each point on the contour will give the same value for the related function. The value of the PAE contours will decrease as the contours move away from the PAE optimum while the value of the ACPR contours will increase as they move away from the ACPR minimum.

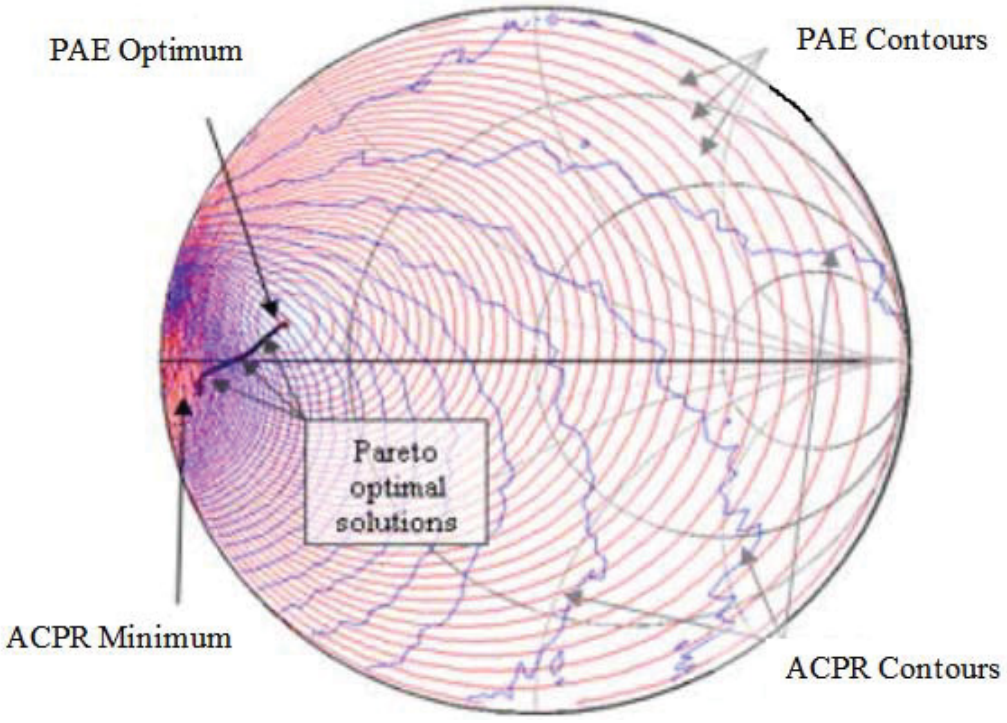

Figure 2.2: PAE and ACPR Contours showing the Pareto Front between the PAE optimum point and the ACPR minimum point. Reprinted from [41]

The Pareto optimum locus [6,7] is shown as the black trace connecting the ACPR minimum and the PAE optimum in Figure 2.2. Each point represents the best PAE possible given a different ACPR limit. The contours differ between devices, but they also change for the same device at different operating frequencies, bias point, and even temperature. The purpose of the reconfigurable matching network is to tune to the Γ_L which provides the best PAE while still meeting an ACPR constraint.

2.2 State of the Art in Reconfigurable Power Amplifiers

This section overviews the literature of past research in the areas of reconfigurable power amplifiers and circuit optimization. The PAE/ACPR circuit optimization techniques in this thesis are based upon gradient-based algorithms that have been demonstrated in previous work. The optimization algorithms shown in Chapters Three and Four are developed and modified from Γ_L searches with a Maury Microwave mechanical tuner [7,8,9,10]. Barkate demonstrates adding input power as a third dimension to create a 3-D power Smith Cube instead of the 2-D Smith Chart [11]. The gradient-based search algorithm can optimize in this 3-D space to optimize another parameter while adding a few measurements to the search. Furthermore, Fellows shows using the bias voltage of the amplifier as the third dimension of a search in the bias voltage Smith Tube [12].

These circuit optimizations were all performed using a traditional mechanical load-pull tuner, which is impractical for use in fast tuning for a practical radar system. The literature shows significant development of fast, reconfigurable tuners for real-time tuning applications. Tunable matching networks using MEMS switches are presented by Yazdani [13], Pesel [14], and Silva Cortes [15]. A varactor-based approach is shown by

Nemati [16]. A combination of these two methods, varactor and MEMS, is shown by Qiao [17]. A genetic algorithm approach is used in matching networks by du Plessis [18].

This thesis synthesizes the gradient search algorithm developed at Baylor by previous students with new tuner technology. The gradient search has been implemented with the Maury mechanical tuner [7], but the tuner is too large and too slow to be practical for real-time optimization. The two tuners discussed in this work are a varactor diode tuner and an evanescent-mode cavity tuner. The search is integrated with these tuners using the fundamental elements of each tuner. This eliminates the need for a tuner characterization and improves the speed of the search compared to the previous mechanical Maury tuner.

2.3 State of the Art in Modeling Weakly Nonlinear Systems

This section discusses the literature references related to the work shown in Chapter Five on Volterra modeling of the memory effects in a weakly non-linear system. The first IEEE paper which used the Volterra series to represent non-linear systems was originally published in 1963 [19]. Since that time, the many papers have been written that utilize the Volterra series to model different non-linear systems for many different applications [20, 21, 22]. Specifically for LNA modeling applications, Zhao and Yu show a modified approach to solving circuit equations for the Volterra kernels of an LNA in [23, 24] respectively. Several techniques published by Silveira [25] and Araujo [26] have been shown to reduce the size of the Volterra kernels, which allows for faster computation of simulation results. Boyd and Bjorsell discuss the direct measurement of the Volterra kernels for a device in [27, 28] respectively. They use three tones to

measure the third-order Volterra kernel, which results in a large number of measurements.

There are several other methods to model memory effects and linearity of LNAs. The work by Kumar in [29] employs an artificial neural network to design a linear LNA for a wide-band transceiver. Nieuwoudt shows numerical design optimization methodology for the design of a wide-band CMOS LNA [30]. Harmonic balance simulation shown by Rizzoli [31] is commonly used to simulate LNA circuits.

This work is a comprehensive study of memory effects on the linearity of wideband LNAs. The thesis builds upon previous work to propose a novel model extraction method for LNAs which will accurately simulate memory effects in the RF passband. The memory effects are simulated to understand the underlying causes of these effects. The Volterra series mathematically describes the memory effects, and a novel approach to extract a Volterra model for an LNA is proposed. This new technique for extracting a Volterra model will reduce the complexity of the testbench setup required to measure the Volterra kernels by reducing the number of tones needed. The proposed technique will also reduce the number of measurements required for model which will save time in the model extraction process as well as reduce the size of the behavioral model for faster simulation time. LNA designers will be able to use this extracted model in a circuit simulation software, such as ADS, to better simulate and account for memory effects on the linearity of their LNA device.

CHAPTER THREE

Varactor Diode Matching Network

The work presented in this chapter has been published in: [33] Z. Hays *et al*., "Real-time amplifier optimization algorithm for adaptive radio using a tunable-varactor matching network," *2017 IEEE Radio and Wireless Symposium (RWS)*, Phoenix, AZ, 2017, pp. 215-217. And in [2] L. Lamers *et al*., "Comparison of bias-voltage and reflection-coefficient based reconfiguration of a tunable-varactor matching network for adaptive amplifiers," *2017 IEEE 18th Wireless and Microwave Technology Conference (WAMICON)*, Cocoa Beach, FL, 2017, pp. 1-5.

Real-time circuitry optimization requires a fast reconfigurable matching network. This chapter discusses a varactor diode approach to reconfigurable matching networks and shows results of several optimization algorithms using a varactor diode tuner.

3.1 Varactor Diode Tuner

A varactor diode matching network was designed and fabricated for use in impedance matching. The capacitance of a varactor diode is dependent on the DC voltage across diode. By manipulating the capacitance of the diode, the input impedance of the matching network can be changed. The matching network presented here is a three element matching network in a tee configuration and is designed to operate at 1.3 GHz center frequency. Figure 3.1 shows the schematic of the varactor diode matching network.

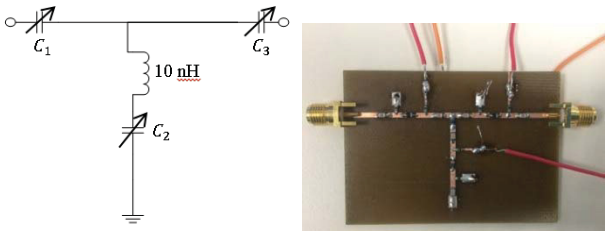

(a) (b)

Figure 3.1: (a) Schematic of the varactor diode matching network. (b) Implemented 1.3 GHz matching network. C_1, C_2, and C_3 are the varactor diodes.

Impedance tuning on a Smith Chart can be achieved by tuning the voltages across the diodes. The Smith Chart coverage of the matching network is shown in Figure 3.2 below.

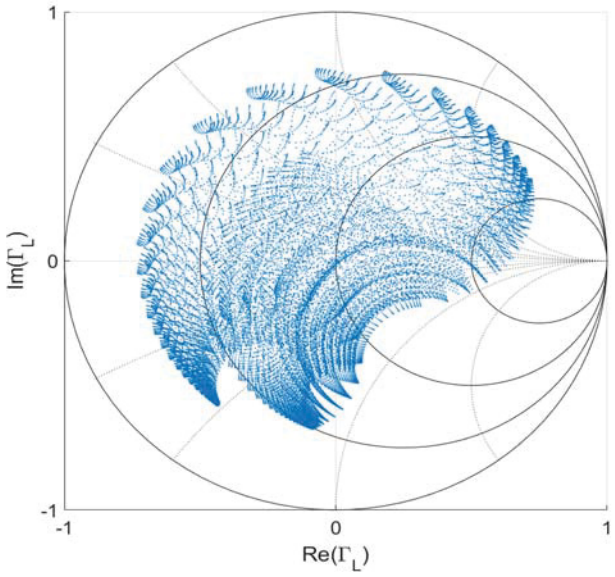

Figure 3.2: Smith Chart coverage of the varactor matching network.

Each of the points shown in Figure 3.2 is the Γ_L corresponding to a different voltage combination. The characterization of the tuner demonstrates a large coverage of the Smith Chart.

3.2 PAE and ACPR Smith Chart Load Pulls

Load pull measurements are the common technique for determining the optimum Γ_L for PAE or ACPR performance. A load pull measures the value for a given parameter, such as PAE, for a large sample of Γ_L and then plots the results as PAE contours in the Smith Chart. The PAE and ACPR load pull contours are shown in Figures 3.3 and 3.4 respectively.

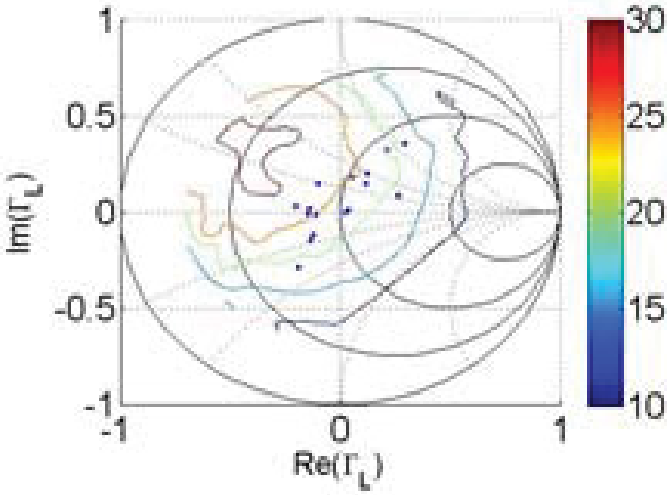

Figure 3.3: PAE load pull of the MWT-173 amplifier using the varactor tuner.

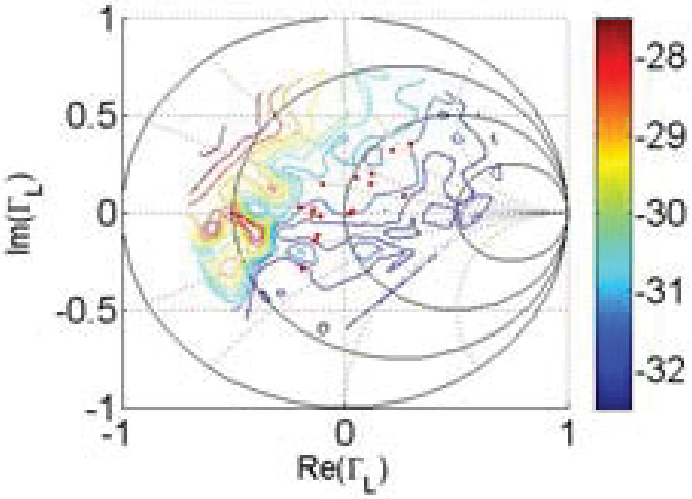

Figure 3.4: ACPR load pull of the MWT-173 amplifier using the varactor tuner.

The load pulls can be interpreted as an exhaustive search for the Γ_L which will obtain the optimum PAE and ACPR for an amplifier. However, the load pull measurementstake a long time due to the huge number of measurements required which is not feasible in a real-time optimization. A fast gradient-based search algorithm has been shown in [32] to find the PAE optimum with an ACPR constraint in the Smith Chart. The impedance search in the Smith Chart requires a characterization between Γ_L and the bias voltages.

3.3 Optimization Algorithm in the Voltage Space

The Γ_L to voltage characterization look-up adds time to the search for each measurement, and any perturbation to the tuner can shift the characterization so that the tuner is not tuning as precisely. To counter this issue, the idea is to directly optimize the PAE and ACPR in the voltage search space instead of using a characterization to convert the voltages to reflection coefficients. The varactor diode matching network has three tuning diodes so the search is a three-dimensional search in the voltage space compared to the two-dimensional search in the Smith Chart plane.

3.4 Search Algorithm

The search algorithm used in the voltage space is a gradient-based constrained optimization shown in [7]. The search measures the PAE and ACPR at a candidate and three neighboring points as shown in Figure 3.5 below.

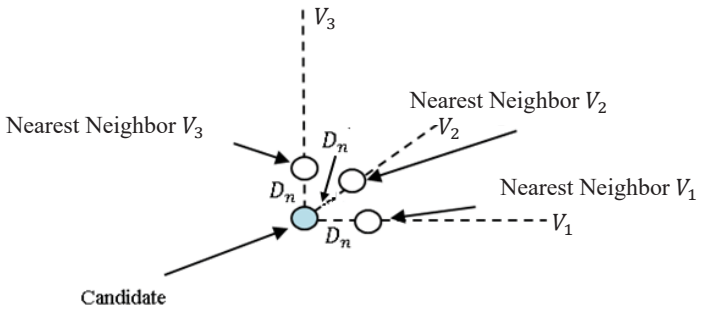

Figure 3.5: Process for determining the gradient in the bias voltage search.

The search measures the PAE and ACPR at a candidate point and three neighboring points. The gradient of the PAE and ACPR can be determined by the values measured at these four points. The algorithm can determine the optimum PAE direction for the unit vector ($\hat{p}$) and optimum ACPR direction with unit vector ($\hat{a}$). The unit vector bisector ($\hat{b}$) bisects $\hat{p}$ and $\hat{a}$. The vector to the next candidate is given by

$$\bar{v} = \hat{a}D_a + \hat{b}D_b \tag{3.1}$$

where the D_a and D_b are coefficients calculated by

$$D_a = \frac{D_s}{2}\frac{|ACPR_{meas} - ACPR_{target}|}{|ACPR_{worst} - ACPR_{target}|} \tag{3.2}$$

and

$$D_b = \frac{D_s}{2}\frac{|\theta_{meas} - \theta_{target}|}{\theta_{target}}. \tag{3.3}$$

The $ACPR_{meas}$ is the ACPR value at the current candidate. $ACPR_{target}$ is the limit set by the user to constrain the search. $ACPR_{worst}$ is the highest ACPR measured up to the current point in the search. For a Pareto-optimum solution, the $\theta_{target} = 90°$ where θ is defined as the angle between $\hat{a}$ and $\hat{b}$. The θ_{meas} is the measured θ at the current candidate. Figure 3.6 shows the two cases for choosing the next candidate. The first case

is when the search is outside the ACPR acceptable region, and the second case is when the search is inside the ACPR acceptable region.

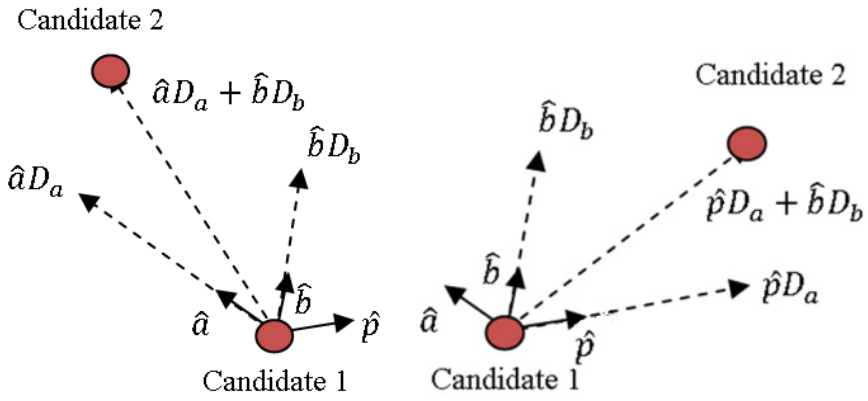

Figure 3.6: Process for determining next candidate: (a) If Candidate 1 is out of compliance with the ACPR limit, the search trajectory will go towards the ACPR acceptable region and the bisector. (b) If Candidate 1 is in compliance with the ACPR limit, the search trajectory will go towards the PAE optimum and the bisector. Reprinted from [7]

3.5 Results

This gradient search algorithm was implemented in the varactor bias voltage space on the bench with the varactor matching network and an MWT-173 FET. The MWT-173 was biased at V_{DS} = 4.5V, V_{GS} = -1.5V, and P_{IN} = 14 dBm. The search algorithm used an ACPR limit of 30.5 dBc. The search algorithm was tested extensively. Figure 3.7 shows an example search below.

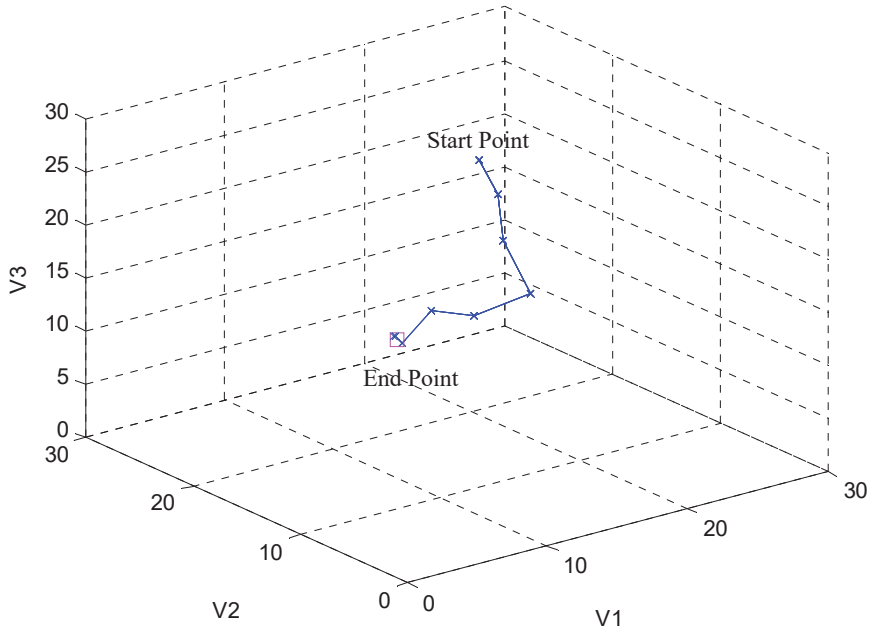

Figure 3.7: Example search started at (22, 22, 22) and ended at (21.11, 16.80, 10.93) with PAE = 26.02% and ACPR = -30.97 dBc.

The search starts at the point $V_1 = 22V, V_2 = 22V, V_3 = 22V$. The search measures a candidate and three neighboring points at each blue 'x' in Figure 3.7 above. The search converges to the red square at $V_1 = 21.11V, V_2 = 16.80V, V_3 = 10.93V$ with PAE = 26.02% and ACPR = -30.97 dBc which is in compliance with the -30.5 dBc ACPR constraint imposed upon the search. Even though the search starting location is far from the optimum, the search takes a fairly direct path to the optimum location with a small number of measurements. The gradient search in the Γ_L Smith chart was implemented on the bench by Luci Hays. For comparison, the Γ_L search took an average of 3.5s per measurement while the voltage search only takes 2.5s per measurement. This time savings is due to the Γ_L search requiring a table lookup for each measurement.

Table 1 shows a compilation of optimizations all starting from different locations in the voltage search space.

Table 3.1: Compilation of Search Results of Control Voltage Tuning. Published in [2].

Start V_1 (V)	Start V_2 (V)	Start V_3 (V)	Final V_1 (V)	Final V_2 (V)	Final V_3 (V)	End PAE (%)	End ACPR (dBc)	# Meas.	Avg. time per meas. (sec)
1	1	1	5.14	1.70	13.68	28.35	-31.11	16	2.46
2	2	2	5.52	0.11	11.34	27.99	-31.26	29	2.47
3	3	3	5.78	2.98	11.20	27.04	-31.36	20	2.52
4	4	4	4.79	1.55	12.60	28.55	-31.01	25	2.46
5	5	5	5.75	1.01	10.74	27.93	-31.46	25	2.53
6	6	6	4.57	0.00	15.07	29.63	-30.53	19	2.46
7	7	7	5.06	0.18	11.66	28.14	-31.06	52	2.50
8	8	8	5.34	0.64	13.89	27.23	-31.11	34	2.48
9	9	9	12.53	14.10	6.98	26.94	-30.53	25	2.49
10	10	10	12.65	14.73	7.26	26.95	-30.80	29	2.50
11	11	11	12.34	15.74	9.01	26.46	-30.59	40	2.50
12	12	12	12.09	15.62	8.45	26.90	-30.52	33	2.49
13	13	13	12.23	16.05	9.76	26.98	-30.75	81	2.46
14	14	14	12.65	15.55	8.63	26.63	-30.98	53	2.47
15	15	15	11.52	14.68	7.60	26.60	-30.91	25	2.47
16	16	16	12.36	15.30	7.78	26.93	-30.54	53	2.47
17	17	17	13.54	15.69	8.64	25.85	-30.84	16	2.47
18	18	18	12.28	16.23	9.70	26.02	-30.79	41	2.46

The searches all converge within the ACPR limit and with PAE between 25.85-29.63%. It is interesting to note, however, that searches 1-8 converged at much different final voltages than searches 9-18. This is due to the voltage space being multimodal. For each impedance, there are several combinations of voltages which plot to that same point on the Smith Chart. Figure 3.8 shows the two PAE modes in the voltage space and where the searches end up in both modes.

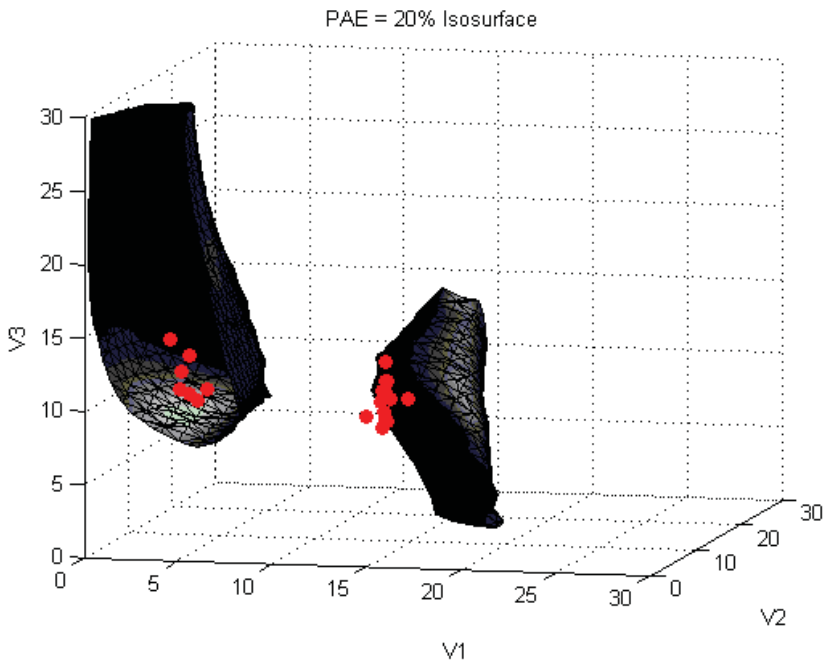

Figure 3.8: PAE = 20% Isosurface with search end points plotted in red.

The two surfaces show where the two modes of the voltage space are located. Both modes in the voltage space plot to the same impedance on the Smith Chart which is why the end values for PAE and ACPR are extremely close. This multimodality is not a problem with the search. Both voltage optimum locations have the same impedance, and the impedance is what determines the PAE and ACPR.

The gradient search algorithm implemented on the varactor diode tuner in the voltage space demonstrates the ability to quickly converge to a constrained PAE operating point. The search in the voltage space instead of the Smith Chart eliminates the need for a characterization and saves look-up time for each measurement in the search.

CHAPTER FOUR

Tuning with the Evanescent-Mode Cavity Tuner

The work in this chapter has been published as: [3] Z. Hays *et al*., "Fast amplifier PAE optimization using resonant frequency interval halving with an evanescent-mode cavity tuner," *2017 Texas Symposium on Wireless and Microwave Circuits and Systems (WMCS)*, Waco, TX, 2017, pp. 1-3. And as [42] Z. Hays et al., "Fast impedance matching using interval halving of resonator position numbers for a high-power evanescent-mode cavity tuner," 2018 IEEE Radio and Wireless Symposium (RWS)

Power handling capabilities of tunable matching networks is one of the limitations in the state of the art, including the varactor matching network. Radar requires very high transmit power to detect targets at long distances. The varactor network was shown by Hays [32] to need a power-dependent characterization for Smith Chart tuning, but varactor diode technology is still limited in its power handling. A new technology needs to be developed to have a significant jump in high power matching network technology.

4.1 Evanescent-Mode Cavity Tuner

A new high power tuner has been shown in [33] to handle up to 90W of power. This is a two element evanescent-mode cavity based tuner. The schematic is shown in Figure 4.1 below.

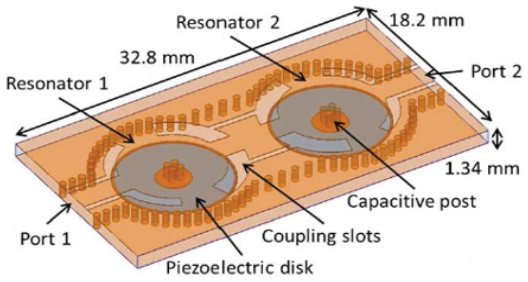

Figure 4.1: Schematic of the evanescent-mode cavity tuner. Shown in [33].

The tuning is performed by changing the voltages of each piezoelectric disks. This changes the height of the cavity, which changes the capacitance of the cavity. By adjusting the capacitance of each cavity, the tuner can cover a large portion of the Smith Chart. The tuner was designed, simulated, and implemented for a center frequency of 3.3GHz. Simulation and measurement of the interval halving and gradient searches will be shown in the following sections.

4.2 Simulated PAE and ACPR Load Pulls of Resonant Cavity Space

The characterization of the tuner's cavity position numbers to impedances is a time-consuming process. Each combination of cavity position numbers is selected and the impedance measured on a VNA (Vector Network Analyzer). Depending on the density of the characterization, the characterization can have hundreds to several thousand points.

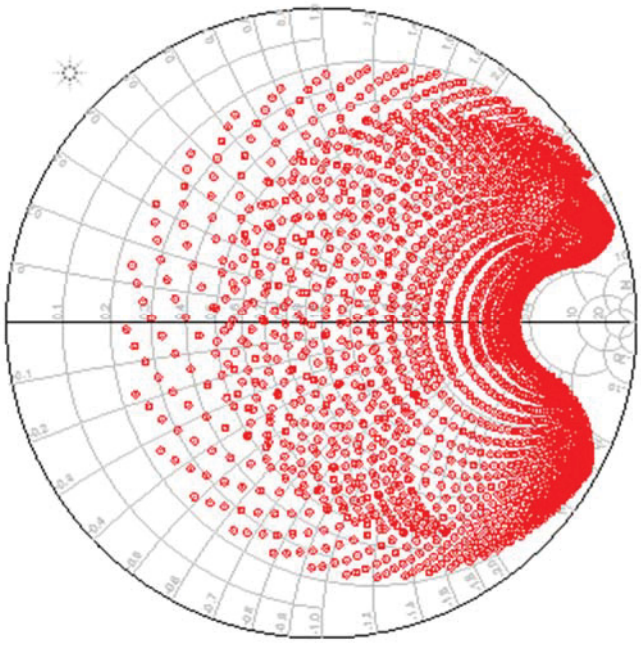

Figure 4.2: Simulated characterization of the cavity tuner

The tuner has also been shown to be vulnerable to physical perturbations. Slight movement or vibrations can cause the tuner's characterization to shift. This means the characterization must be retaken constantly to have an accurate mapping of cavity position numbers to reflection coefficients.

A solution to this problem is to tune the cavity position numbers directly in load pulls and searches instead of mapping them to reflection coefficients first. This completely eliminates the need for characterizations, which saves time and is much more reliable. The tuner was simulated in Advanced Design Studio (ADS) with symbolically defined blocks as the tunable position numbers. The tuner model was provided by collaborators at Purdue University.

This simulation model was based upon a simple cylindrical waveguide model for the resonant cavity. A symbolically defined block calculated the resonant frequency of the cavity using the radius and height of the cylinder. The ADS algorithm would change the height of the each cavity to adjust the resonant frequency. The change in resonant frequency would result in a change in reflection coefficient and would tune around the Smith Chart.

Using the ADS model for the tuner, PAE and ACPR load-pull simulations were performed in the resonant cavity position number space. The simulated PAE load pulls in the resonant cavity positions number and Smith Chart are shown in Figure 4.3 and Figure 4.4.

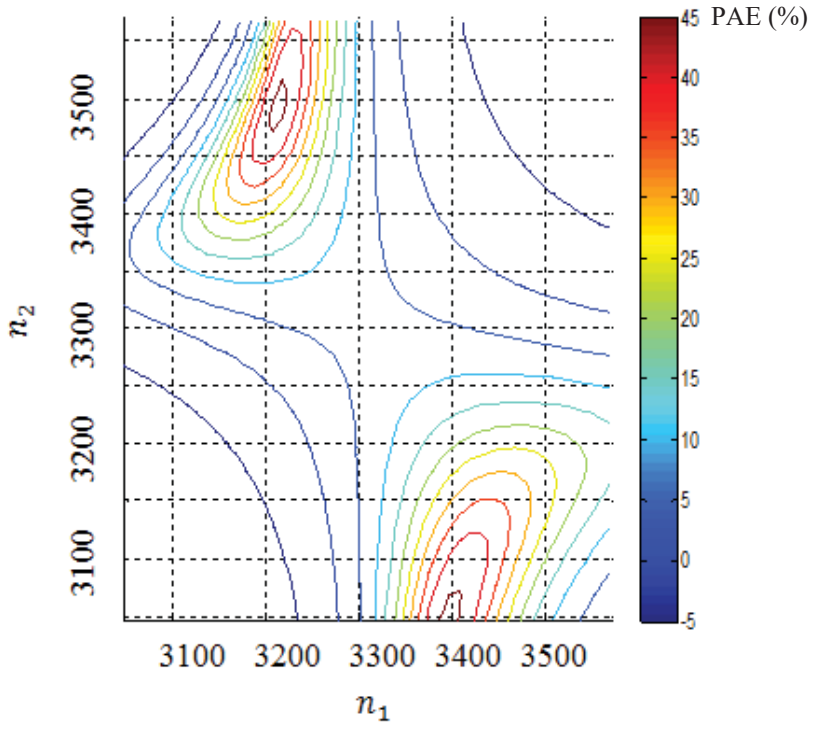

Figure 4.3: Simulated PAE load pull in the cavity position number space

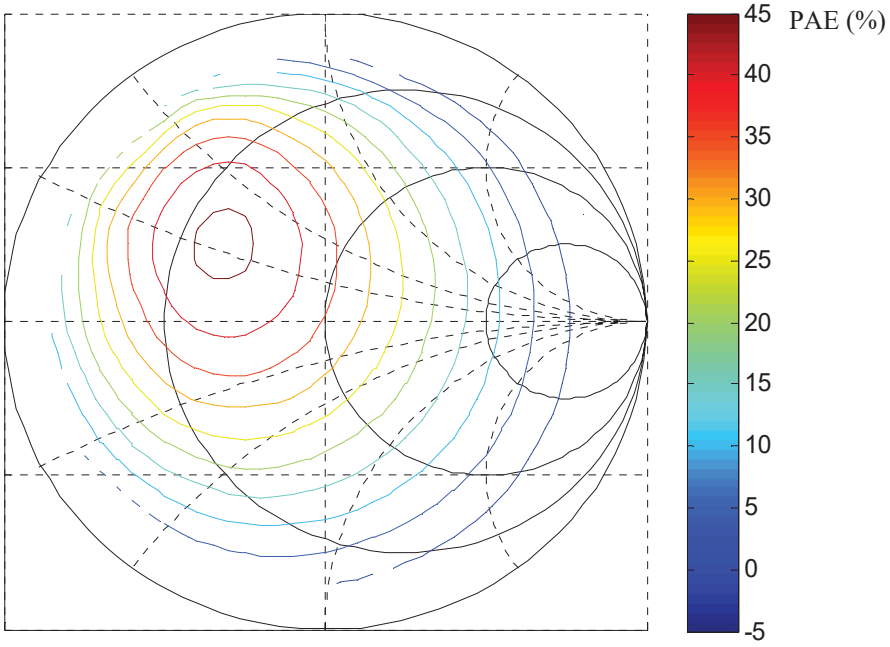

Figure 4.4: Simulated PAE load pull in the Smith Chart

In the cavity position number space, there are two optimum locations. For most optimization algorithms, this would be a problem as the search could get stuck in the local optimum instead of the global optimum. However, both optimums in the cavity position number space plot to the same reflection coefficient in the Smith Chart. It does not matter which optimum the search finds in the cavity position number space since these are the identical reflection coefficient, and the reflection coefficient is what is determining the PAE and ACPR of the device. The load pull for the ACPR is shown for the cavity position number space as well in Figure 4.5.

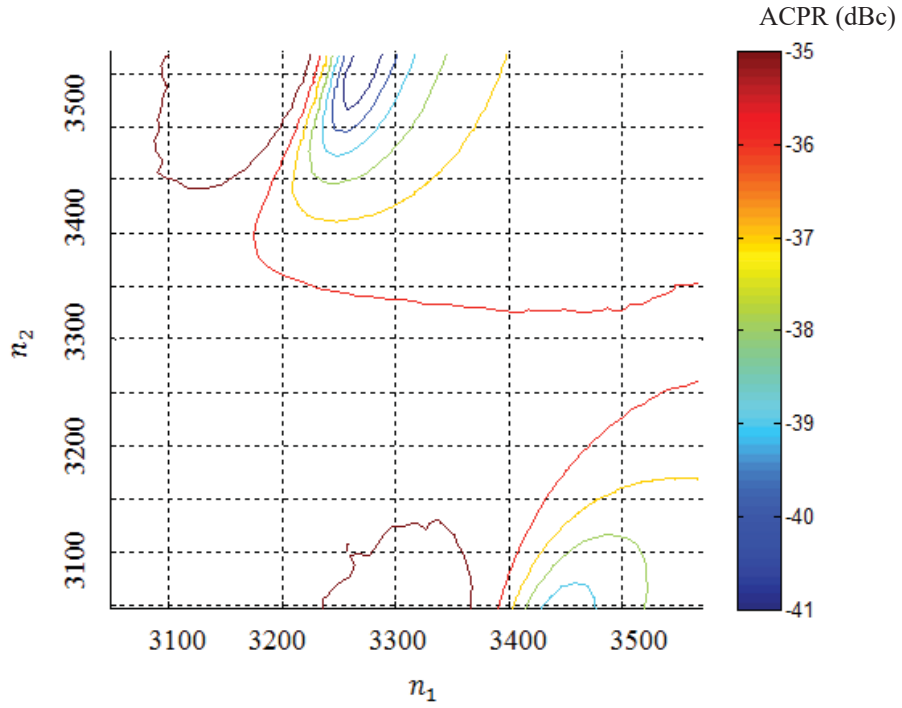

Figure 4.5: Simulated ACPR contours in cavity position number space.

The ACPR contours are also multimodal, but are not quite as symmetrical as the PAE contours. For a stricter ACPR limit, the search may be confined to one of the two PAE optimums.

4.3 2D Position Number Interval Halving PAE Search in Simulation

The simulated tuner was used to implement a simple interval halving PAE search in the cavity position number search space to verify that simulation was working correctly and that the PAE contours in this search space are sufficiently convex for search algorithms to converge consistently.

The interval halving algorithm is a simple search method used to find the max PAE of a device. Figure 4.6 shows the 1D illustration of how the search works.

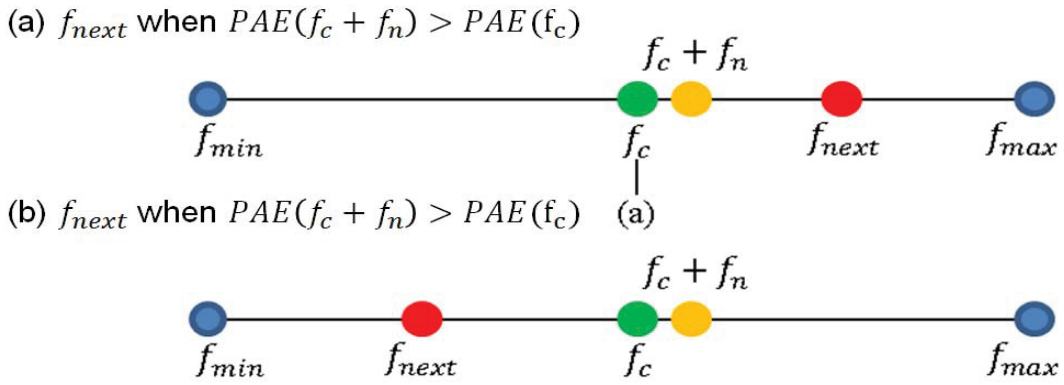

Figure 4.6: Illustration of interval halving search.

The search measures the PAE at a candidate and neighbor slightly above. If the neighbor has better PAE, then the search steps as shown in 4.6 (a) and the new interval is between f_c and f_{max}. If the neighbor has worse PAE, then the search steps as shown in 4.6(b) and the new interval is between f_{min} and f_c. This process is repeated iteratively between n_1 and n_2 until the interval falls under a certain threshold.

The interval halving search was implemented in MATLAB and ADS. An example search is shown below in Figure 4.7.

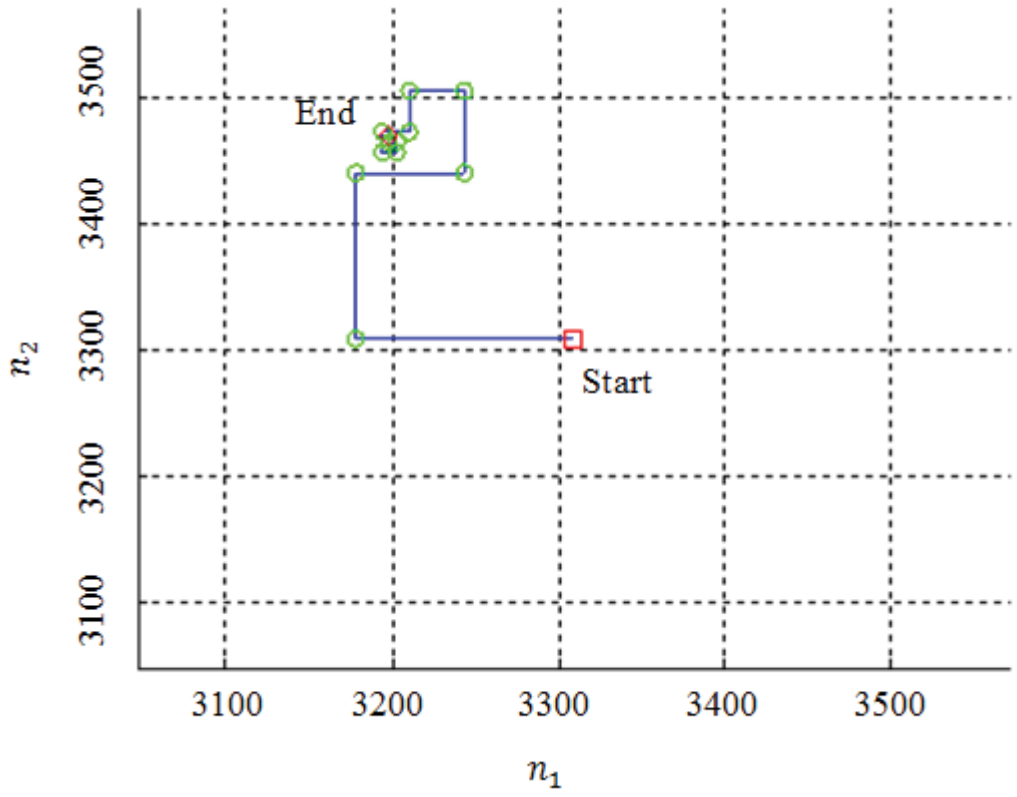

Figure 4.7: Simulated interval halving search with end PAE = 44.93% at $n_1 = 3420, n_2 = 3110$.

The search shows convergence to the top left PAE optimum as shown in the PAE load pull. The success of the simple interval halving algorithm in simulation was a step toward implementing a more advanced search algorithm to find the optimum PAE with an ACPR constraint.

4.4 Two-Dimensional Position Number Gradient Search in Simulation

A gradient search algorithm was implemented in simulation to find the optimum PAE within an ACPR constraint. A gradient-based approach allows for a more direct path to the optimum than the interval-halving method, and an ACPR constraint can be added to ensure no interference with other users in the neighboring frequency bands. The

gradient search implemented is described more fully in Chapter Three. The PAE load pull is shown again for reference in Figure 4.8 as well as two example searches in Figures 4.9 and 4.10.

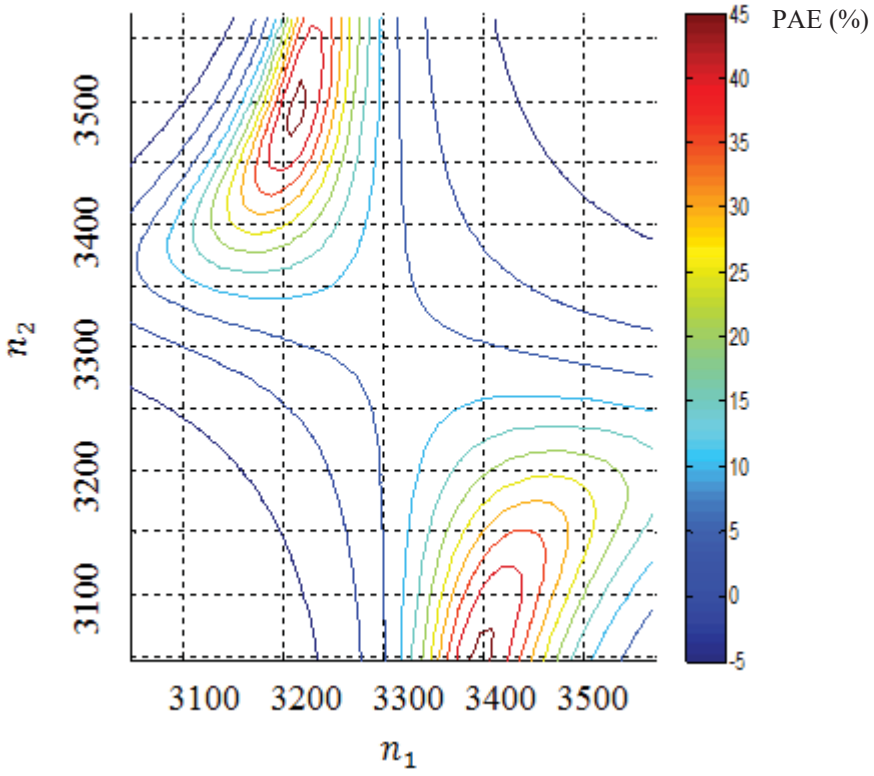

Figure 4.8: Simulated PAE load pull in cavity position number space.

The searches in Figure 4.9 and Figure 4.10 show the algorithm converge to whichever PAE optimum is closest to the starting point. Again, these two optima in the cavity position number space plot to the same impedance so it does not affect the result which optimum the search finds.

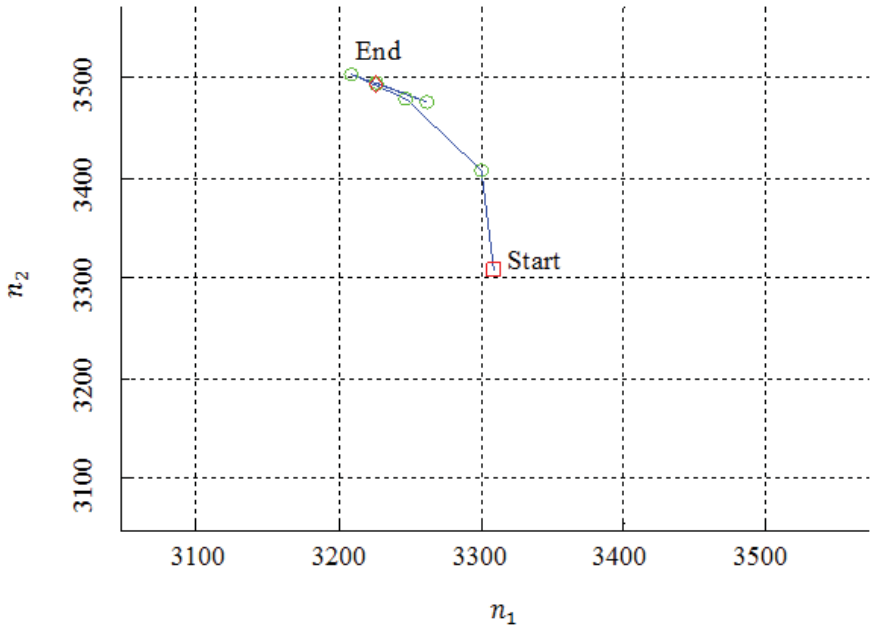

Figure 4.9: Simulated gradient search with end PAE = 43.62% and end ACPR = -38.00 dBc at $n_1 = 3224, n_2 = 3492$. ACPR limit = -38 dBc.

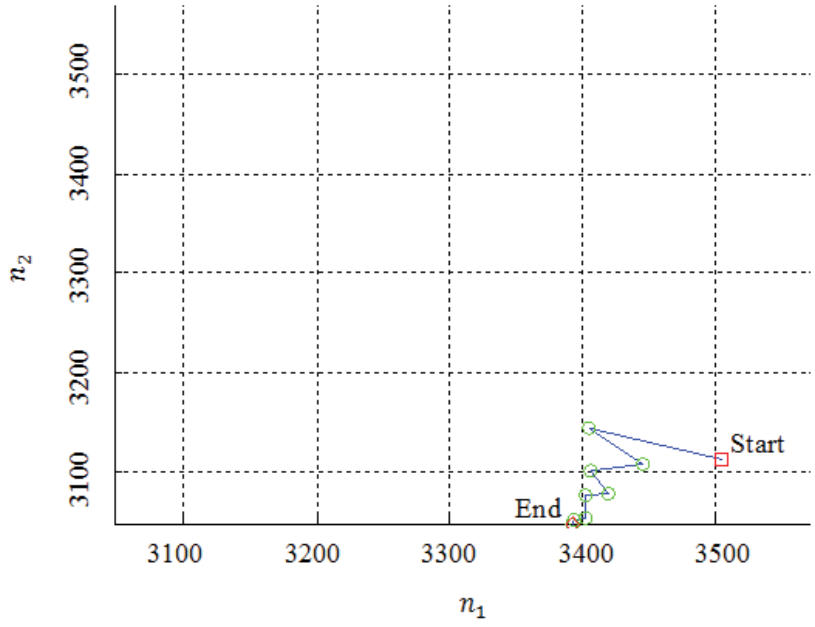

Figure 4.10: Simulated gradient search with end PAE = 45.88% and end ACPR = -36.10 dBc at $n_1 = 3389, n_2 = 3061$. ACPR limit = -36 dBc.

Table 4.1 shows a compilation of eight simulated gradient searches with starting locations spread around the search space.

Table 4.1. Compilation of simulated gradient PAE/ACPR search results with ACPR limit = -36 dBc.

Search #	Start n_1	Start 2	End n_1	End n_2	PAE %	ACPR (dBc)	# Meas.
1	3110	3110	3210	3460	44.39	-36.21	14
2	3510	3510	3200	3480	45.32	-36.09	14
3	3110	3510	3200	3480	45.32	-36.09	14
4	3510	3110	3390	3050	45.94	-36.16	15
5	3110	3310	3390	3050	45.88	-36.10	15
6	3510	3310	3390	3050	45.93	-36.16	17
7	3310	3110	3390	3050	45.93	-36.16	17
8	3310	3510	3390	3050	45.93	-36.16	17

The first three searches ended up in the top left PAE optimum while the last five searches ended up in the bottom right PAE optimum. All eight searches achieved excellent PAE while staying under the ACPR limit of -36 dBc. The simulation results for the interval halving and gradient searches were able to converge consistently. The next step was to implement the searches on the bench in measurement.

4.5 Characterization and load pulls in resonant cavity position number space

The evanescent-mode cavity tuner was placed in the measurement test bench to test how measurements would compare to the simulation results. The characterization of the tuner in measurement is shown below in Figure 4.11.

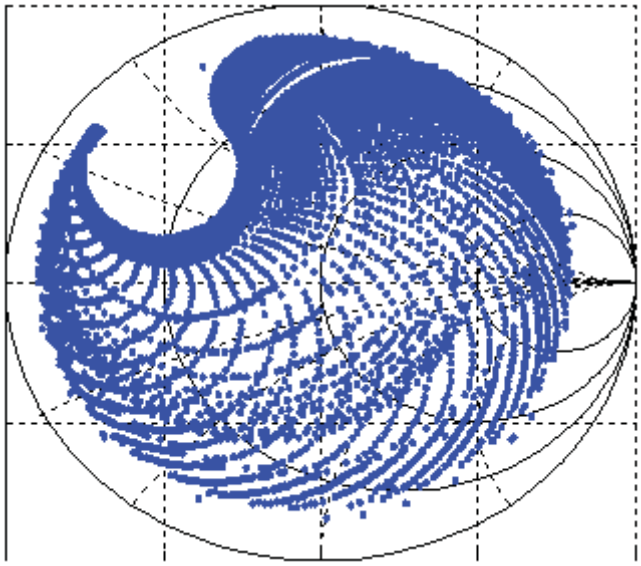

Figure 4.11: Characterization of the tuner at 3.3GHz.

The characterization shows a similar coverage as the simulated characterization which was shown previously, however the small circle where the tuner cannot reach is shifted around the Smith Chart. This is due to transmission lines not included in the ADS tuner model and is not significant. The coverage of the Smith chart can be rotated by simply adding more transmission line. The PAE and ACPR load pulls in the resonant cavity position number search space are shown for the tuner in the following figures. Figure 4.12 shows the PAE load pull contours. Figure 4.13 shows the ACPR load pull contours.

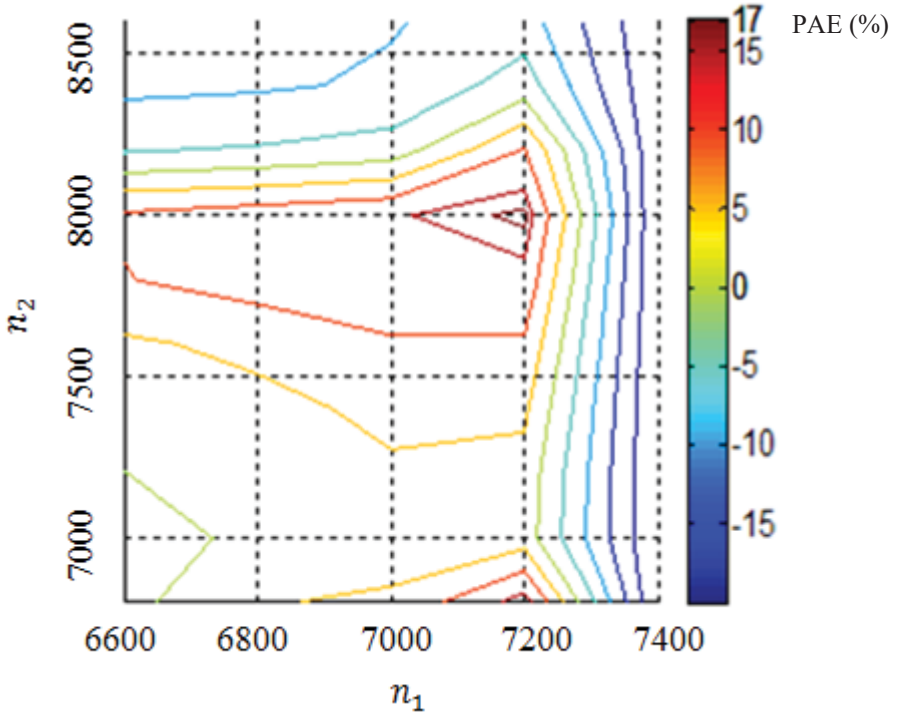

Figure 4.12: Measured PAE load pull of MWT-173 at 3.3GHz.

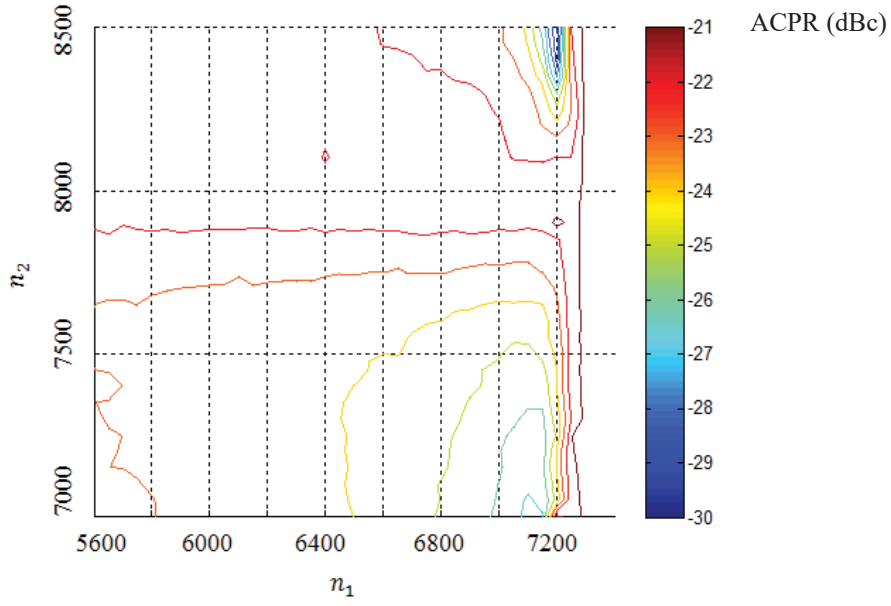

Figure 4.13: Measured ACPR load pull of MWT-173 at 3.3GHz.

The load pulls show that there is only one optimum PAE location as opposed to the two seen in simulation. This is due to the fact that the simulation ADS model is a very simple model. It leaves out parasitic effects and assumes ideal components for each of the two elements. The interval halving algorithm was implemented on the bench to determine how the tuner would perform in measurement.

4.6 Two-Dimensional Interval Halving Search in Resonant Cavity Position Number Space

The PAE interval halving algorithm implemented was the same algorithm as shown in simulation. The search was run multiple times to verify repeatability. The results are shown in the following example and table. Figure 4.14 shows the typical search pattern.

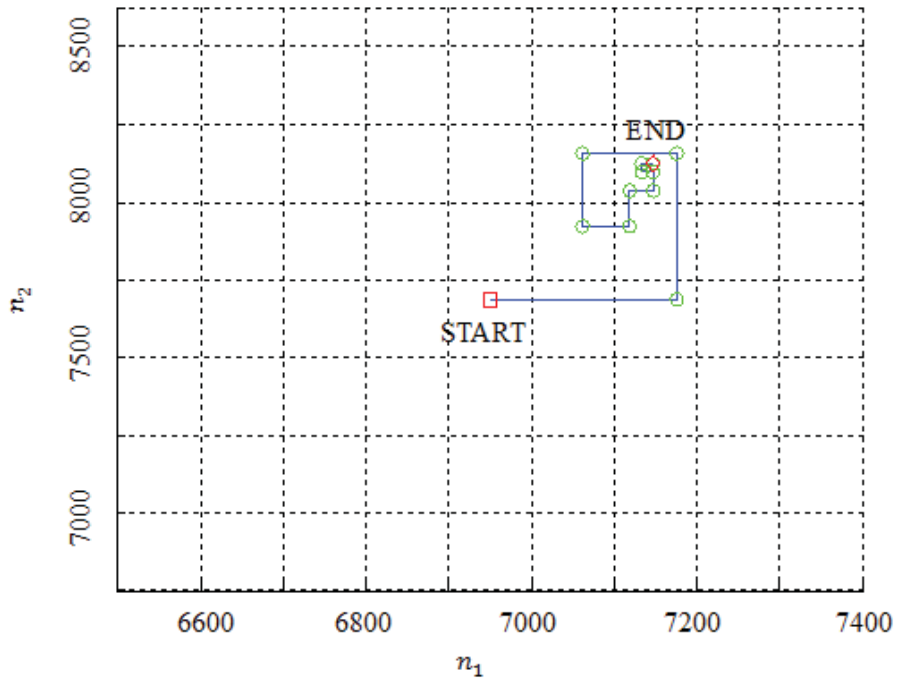

Figure 4.14: Example search with MWT-173 at V_{DS} = 4.5V, V_{GS} = -1.5V, P_{IN} = 14 dBm. Max PAE = 20.78% at $n_1 = 7147, n_2 = 7902$ with 22 measurements.

The search shows a quick convergence to the PAE optimum as shown by the load pull. Table 4.2 shows a compilation of search results below.

Table 4.2. Compilation of Interval Halving PAE Searches

Trial #	End n_1	End n_2	End PAE (%)	# Meas.
1	7161	7948	21.11	22
2	7159	7948	21.04	22
3	7147	7878	20.43	22
4	7147	7902	20.78	22

Each of the searches converges to similar position numbers and PAE with a reasonable number of measurements. Since the interval halving was shown to be successful on the bench, the next step was to implement the gradient search on the bench.

4.7 Two-Dimensional Gradient Search in Resonant Cavity Position Number Space

The cavity position number gradient search was implemented in measurement with the evanescent-mode cavity tuner. The gradient-based approach, previously described in detail in Chapter Three, takes a more direct path to the PAE optimum, and also allows for an ACPR constraint to be added to the optimization process. The gradient search requires a neighboring point to be taken in each dimension while the interval halving only takes one neighboring point per candidate. Despite this, the gradient search will usually converge with a smaller number of measurements than the interval halving search since the gradient search takes a more direct to the optimum point. The PAE load pull with the ACPR constrained region is shown below in Figure 4.15.

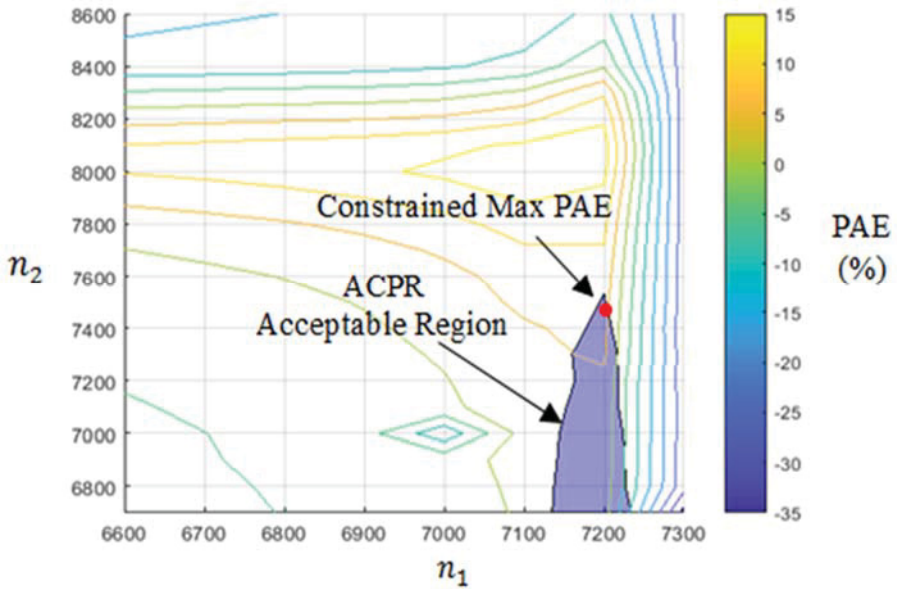

Figure 4.15: PAE load pull with ACPR acceptable region of ACPR < -28 dBc with MWT-173 FET. Constrained PAE optimum: PAE = 7.22%, ACPR = -28.09 dBc at $n_1 = 7200$, $n_2 = 7500$.

In practice, it was shown by my colleague, Sarvin Rezayat, that the gradient search has trouble converging from starting points far away from the optimum location. This is because the PAE contours are not convex as they are in the Smith Chart. As such, one of the challenges to doing the search in the resonant cavity position number space is to begin the search at a point where the gradient vectors will lead the search to the correct optimum. Sarvin demonstrated that by measuring five different candidates around the search space, the best point could be chosen as a good starting candidate for the gradient search. This technique, known as Sarvin's method, adds five extra measurements at the beginning of the search, but averages fewer measurements per search and converges more consistently due to starting near the optimum location.

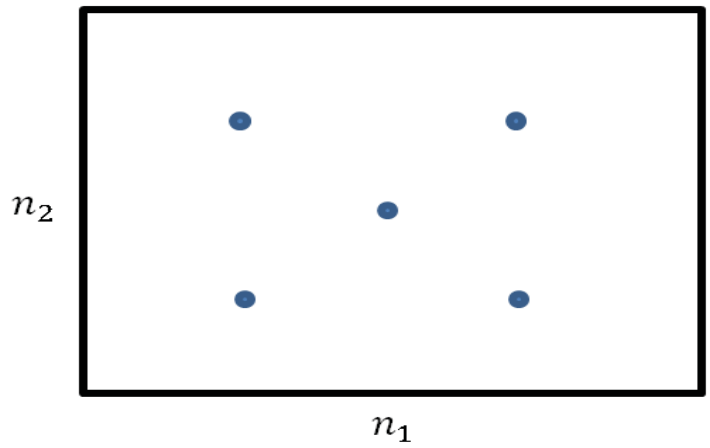

Figure 4.16: Sarvin's Method: Measure five different candidates to choose a good start candidate for the gradient search. First shown in [43].

The gradient search was implemented with Sarvin's method and the results are shown in an example search below in Figure 4.17. Table 4.3 shows a compilation of several different searches.

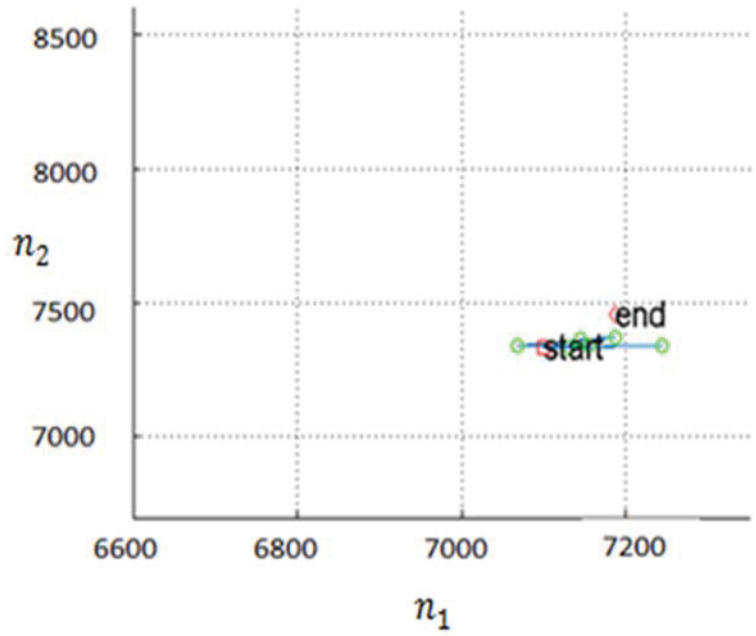

Figure 4.17: Example gradient search with ACPR limit = -28 dBc. End PAE = 7.92%, End ACPR = -28.18 dBc at $n_1 = 7188$, $n_2 = 7456$ with 25 measurements.

This example shows the search starting from the bottom right candidate of the five starting candidates which was near the optimum location. The following table shows a compilation of searches.

Table 4.3. Compilation of PAE/ACPR Gradient Searches with ACPR Limit = -28 dBc.

Search #	Start n_1	Start n_2	Start PAE	Start ACPR	End n_1	End n_2	End PAE	End ACPR	Total # Meas.
1	7100	7333	3.86	-25.02	7179	7445	7.63	-28.24	13
2	7100	7333	3.82	-26.23	7476	7454	7.86	-28.08	16
3	7100	7333	3.75	-26.24	7176	7440	7.70	-28.15	25
4	7100	7333	3.75	-26.19	7171	7419	7.37	-28.19	25
5	7100	7333	3.69	-26.28	7177	7408	7.35	-28.23	25
6	7100	7333	3.70	-26.31	7173	7433	7.51	-28.08	25
7	7100	7333	3.68	-26.18	7187	7452	7.87	-28.21	22
8	7100	7333	3.67	-26.13	7188	7451	7.87	-28.23	28
9	7100	7333	3.65	-26.13	7188	7456	7.92	-28.18	25
10	7100	7333	3.80	-26.14	7189	7450	7.91	-28.35	22
Average			3.74	-26.08	7180.4	7440.8	7.70	-28.19	22.6
Standard Deviation					6.9	16.16	0.22	0.08	4.65

The table shows that the gradient search converges at an average of 22.6 measurements while the interval halving search took a very similar 22 measurements per search. The gradient search is also able to constrain the ACPR of the DUT which allows for useful optimizations.

4.8 Input Power Added in a Three-Dimensional Gradient Search in Resonant Cavity Number Space

The next step after the 2D gradient search in resonant cavity position number space was to add another dimension in the search space for a more finely tuned optimization result. The input power to the DUT is added to the two-dimensional cavity

position number (n_1, n_2) plane to make a three dimensional search space. This is visualized in the following figure.

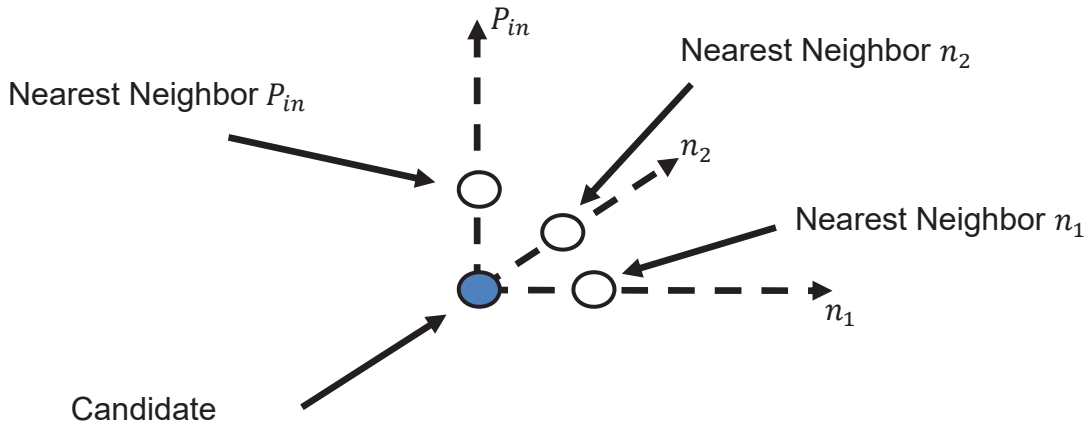

Figure 4.18: 3D Gradient search illustration. Candidate with 3 neighbors.

The addition of another dimension to the search requires another neighbor to be measured for each candidate. This increases the number of measurements per search, but allows for simultaneous optimization of the load reflection coefficient and input power.

The best starting position of the gradient search also had to be found for the 3D search. Sarvin's Method is implemented in the position number plane at the lowest input power level. Since there is low input power, the candidates will meet the ACPR limit. Once Sarvin's method determines the best candidate in the position number plane, the input power is increased incrementally until the candidate reaches the ACPR limit. The gradient search then begins at this point, which is typically near to the optimum in all three dimensions. This three-dimensional, modified Sarvin's method is illustrated Figure 4.19 below.

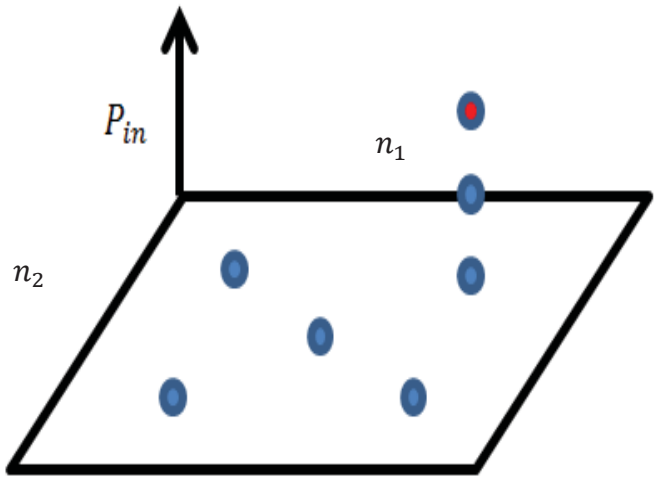

Figure 4.19: Choosing best starting position for 3D input power search

Figure 4.19 shows the search choosing the top right point in the (n_1, n_2) plane, and stepping up to start the gradient search at the red point.

Load pulls were run at different P_{IN} values to generate a 3D visualization of the search space. Figure 4.20 shows the search space with the ACPR limit surface and the optimum constrained PAE surface. Below the blue ACPR surface contains the acceptable ACPR region. The red PAE surface is the max constrained PAE surface that intersects the blue ACPR limit surface at the one green point. This green point is the constrained maximum PAE point. The gradient search should converge to near this green point and achieve a constrained PAE near the 9.86% PAE that the load pull found as the optimum.

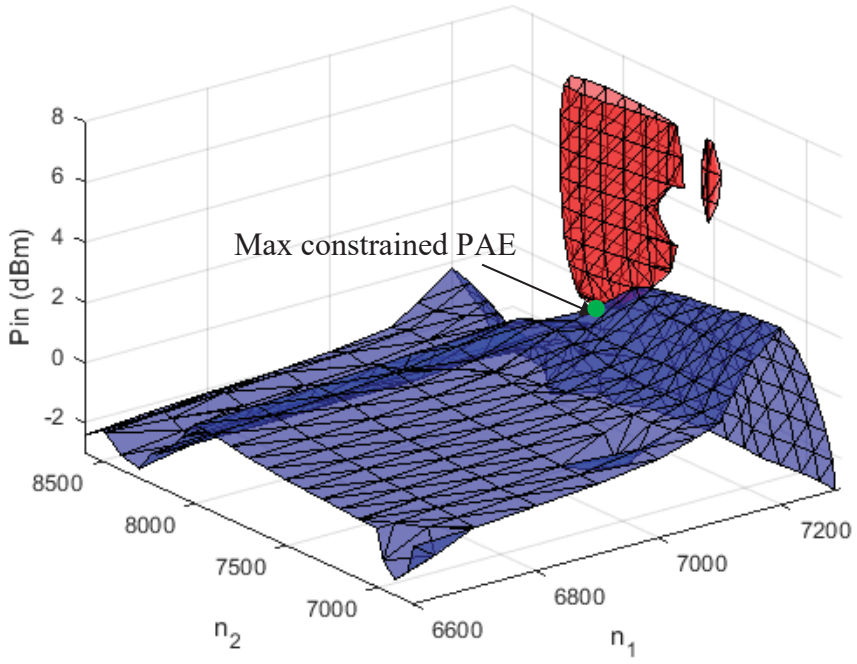

Figure 4.20: ACPR = -25 dBc surface (blue) and max constrained PAE = 9.86% surface (red). Green dot is the point of intersection where the constrained PAE optimum is located: Maximum constrained PAE: 9.86% at n_1 =7200, n_2 = 7700.

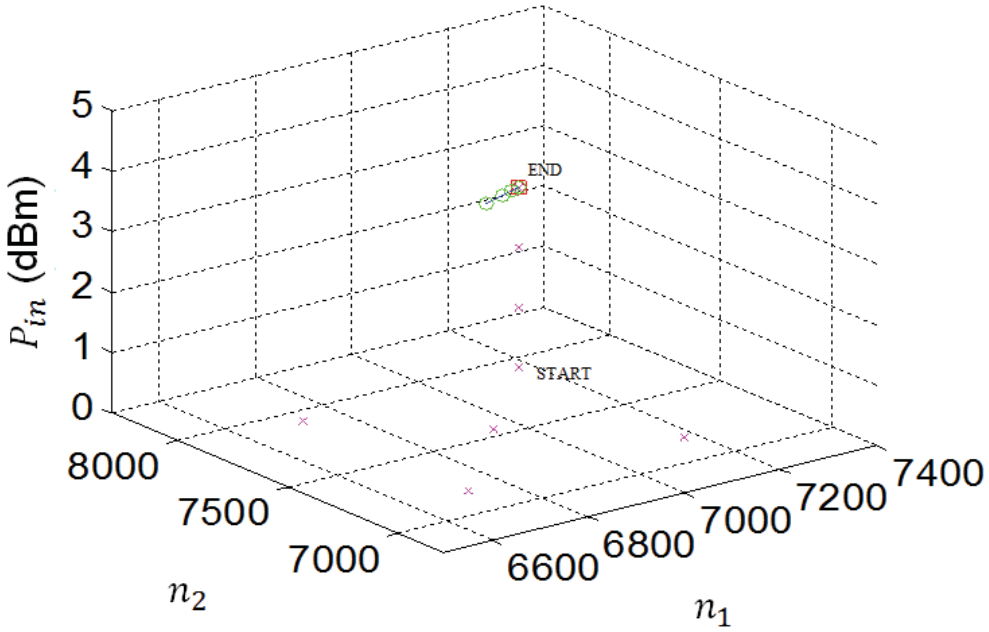

Figure 4.21: Example of 3D gradient search Skyworks amplifier. End PAE = 9.04% and End ACPR = -25.83 dBc at n_1 =7175, n_2 = 7925, P_{in} = 3.00 dBm with ACPR limit = -25 dBc.

Figure 4.21 shows the search choosing the top right of the five starting locations in the (n_1, n_2) plane, stepping upward in P_{IN},and beginning the search very near the optimum so that few additional measurements were required to finely tune the end point. Table 4.4 shows a compilation of search results.

Table 4.4: Compilation of 3D P_{IN} Gradient Searches

Search #	Start n_1	Start n_2	Start P_{in} (dBm)	End n_1	End n_2	End P_{in} (dBm)	End PAE (%)	End ACPR (dBc)	# Meas
1	6950	7550	0	7184	7866	2.25	9.46	-26.53	28
2	6950	7550	0	7184	7921	2.46	9.70	-25.35	32
3	6950	7550	0	7192	7793	3.01	9.73	-25.55	19
4	6950	7550	0	7195	7737	2.83	9.31	-26.26	32
5	6950	7550	0	7192	7824	2.94	9.78	-25.22	19
AVG	-	-	-	7189	7828	2.70	9.60	-25.78	26

The searches all converge below the ACPR limit of -26 dBc and achieve PAE values close to the 9.86% as found by the exhaustive load pull. This indicates the search consistently performs well.

4.9 Three-Dimensional Gradient Search in Resonant Cavity Number Space with Gate Voltage as the Third Dimension

Many different parameters can be used as the third dimension for the cavity position optimization in place of input power. The gate voltage of the DUT was also used as the z-axis dimension of the search. Instead of P_{IN}, the V_{GS} of the amplifier became the third dimension of the search.

For P_{IN}, it is often reasonable to start with the five candidates in the (n_1, n_2) plane at the lowest P_{IN} value because this keeps the beginning of the search within the ACPR

acceptable region. For V_{GS}, however, there is no way to know where the ACPR acceptable region is located. When there is no *a priori* knowledge of the search space for a gradient search, it is typically a good choice to start in the middle of the search space. So for the V_{GS} cavity position cube, the search starts with five points in the (n_1, n_2) plane at the center V_{GS} value.

Similar to the P_{IN} search, load pulls were run at varying levels of V_{GS} to create a visualization of the three-dimensional search space. The results are shown in Figure 4.22 and Figure 4.23.

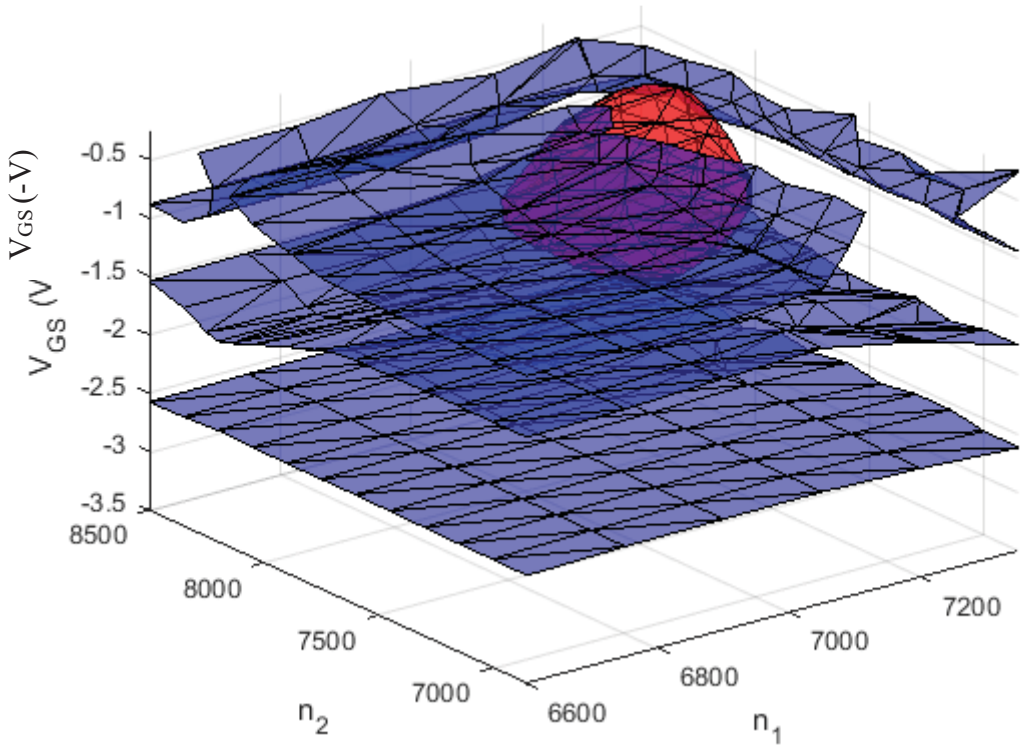

Figure 4.22: ACPR = -23 dBc surfaces (blue) and max constrained PAE = 13.07% surface (red).

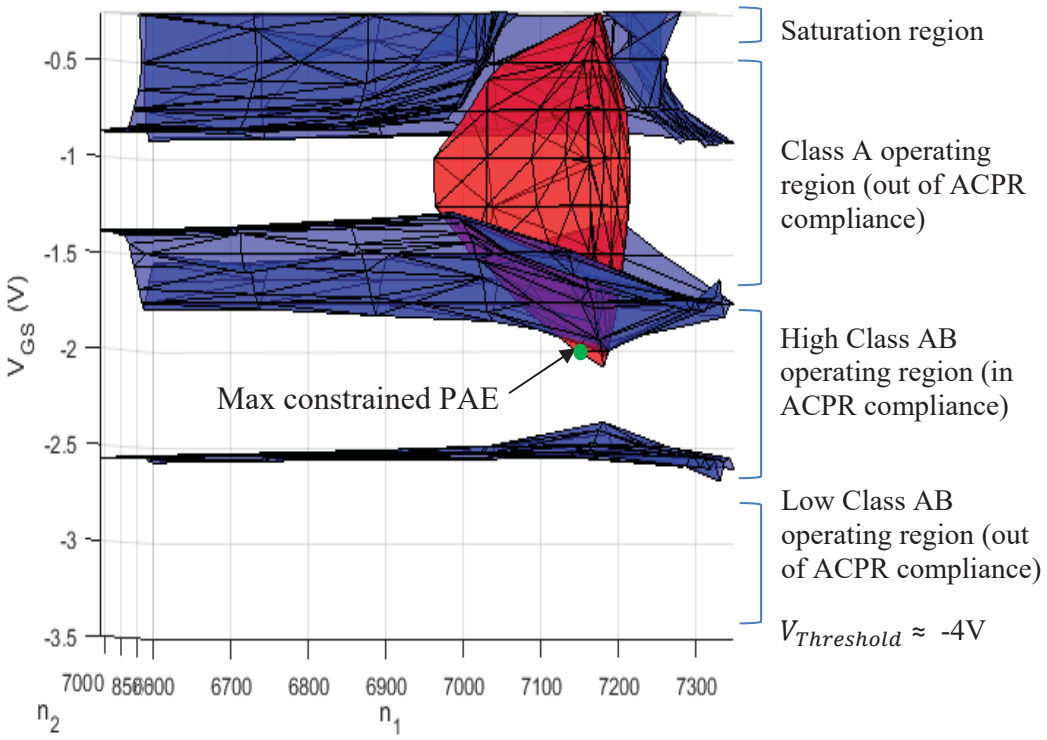

Figure 4.23: ACPR = -23 dBc surfaces (blue) and max constrained PAE = 13.07% surface (red).

The output signal is in the ACPR acceptable region for -2.5V < V_{GS} < -1.5V when the amplifier is at a Class AB bias point. The PAE max constrained surface is located above that where the amplifier is at a Class A bias, and intersects the ACPR limit at the green dot in Figure 4.23. Typically, a Class B or Class AB will perform more nonlinearly and therefore more efficiently than a Class A bias. However, Figure 4.23 shows that the MWT-173 device is pushed into nonlinear operation at large values for V_{GS}. The likely reason for this behavior is that the input power to the device is held constant for all the three-dimensional load pull. As V_{GS} is lowered, the PAE drops significantly. A Class B bias requires a larger input power than a Class A bias to push the device into compression and reach higher PAE. Figure 4.23 shows that for a Class A

bias, the input power is sufficient to cause nonlinear behavior, but for the Class AB bias, the input power is not large enough to cause significant nonlinearity. The ACPR is out of compliance at a Class B bias because of signal clipping where V_{GS} is below -2.5V. As V_{GS} increases, the gain of the amplifier increases. This lowers the ACPR so that between V_{GS} = -2.5V and V_{GS} = -1.5V, the device is in ACPR compliance. It is likely that when V_{GS} > -1.5V, then the amplifier is pushed more into compression. The resulting intermodulation terms cause the ACPR to go out of compliance.

The three-dimensional search algorithm was run multiple times to ensure repeatability. An example search is shown below in Figure 4.24.

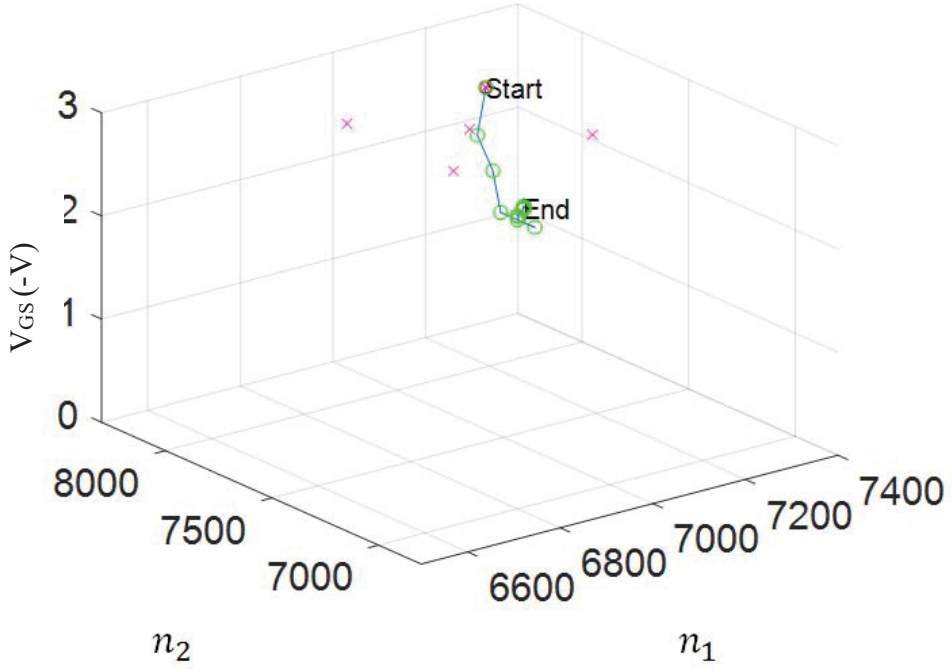

Figure 4.24: Example search converged at n_1 =7183, n_2 = 7802, V_{GS} = 3.00 dBm, with PAE = 10.94% and ACPR = -23.11 dBc. ACPR limit = -23 dBc.

A compilation of searches is shown in Table 4.5. Searches 1 through 5 were performed with starting = -1V, searches 6-10 were taken with starting V_{GS} = -2V, and searches 11 through 15 were performed with starting V_{GS} = -3V. All the searches

achieved fairly good PAE while staying within the ACPR constraint. The maximum constrained PAE found by the exhaustive load pulls was 13.07%. Only three of the fifteen searches were able to achieve a constrained PAE above 13%. This indicates that while the search consistently gets close to the optimum in (n_1, n_2, V_{GS}), the search struggles to find the precise optimum. It can be noted that the best PAE values had a slightly higher end value for n_2. Also, starting the search at V_{GS} = -2 V results a smaller number of measurements and more consistent PAE convergence. This shows that starting in the middle of the search space works best for the gradient search.

Table 4.5. Compilation of 3D V_{GS} Gradient Searches

Search #	Start n_1	Start n_2	Start V_{GS} (V)	Start PAE (%)	Start ACPR (dBC)	End n_1	End n_2	End V_{GS} (V)	End PAE (%)	End ACPR (dBc)	Total Meas.
1	6950	7550	-1	1.14	-21.11	7186	8277	-1.87	9.95	-25.05	39
2	6950	7550	-1	1.24	-21.29	7106	7899	-1.73	10.36	-23.04	56
3	6950	7550	-1	0.66	-21.52	7074	8090	-1.87	13.09	-23.03	31
4	6950	7550	-1	-0.37	-22.07	7126	7996	-1.84	13.42	-23.04	56
5	6950	7550	-1	-0.26	-21.62	7128	7948	-1.80	12.36	-23.04	68
6	6950	7550	-2	-5.83	-29.24	7164	7851	-1.79	11.79	-23.03	28
7	6950	7550	-2	-5.76	-29.29	7157	7878	-1.79	12.25	-23.00	36
8	6950	7550	-2	-5.65	-29.19	7165	7834	-1.78	11.53	-23.03	28
9	6950	7550	-2	-5.71	-29.29	7166	7859	-1.80	12.22	-23.03	32
10	6950	7550	-2	-5.68	-29.24	7163	7853	-1.78	11.89	-23.06	20
11	6950	7550	-3	-43.95	-19.36	7183	7802	-1.74	10.94	-23.11	48
12	6950	7550	-3	-45.48	-18.94	7086	8041	-1.86	12.85	-23.06	32
13	6950	7550	-3	-44.25	-19.09	7110	8045	-1.86	13.57	-23.09	40
14	6950	7550	-3	-45.50	-18.94	7160	7869	-1.77	11.98	-23.07	56
15	6950	7550	-3	-53.67	-19.08	7191	7732	-1.81	10.30	-23.28	36

4.10 Conclusions on Searches in the Resonant Cavity Position Number Space

In both simulation and measurement, the interval halving and gradient search optimizations were able to tune quickly to the point of optimum PAE in the resonant cavity position number space. The gradient search is able to include an ACPR constraint

as well as include more dimensions to the optimization such as P_{IN} and V_{GS} to further improve the performance of the device under test. Searching in the cavity position space eliminates the need for time-consuming characterizations and can self-correct any drift in tuner behavior. The gradient search algorithm has been shown to tune the fundamental elements of the evanescent-mode cavity tuner to enable fast, high-power, tuning capabilities for a radar system.

CHAPTER FIVE

Investigation of Wideband Low-Noise Amplifier Linearity in Receiver Interference Scenarios

This chapter details a study to investigate and model nonlinearities in a broadband, weakly non-linear low-noise amplifier (LNA). There has been a noticed discrepancy between simulation and measurement, specifically with respect to nonlinearities at the third order intermodulation distortion (IMD3) frequencies due to up-conversion of baseband memory effects [34]. Once these nonlinearities had been identified, a solution and test plan were developed to give designers a method to better model an LNA and be able to produce a simulation tool that will more closely match measurements. The Volterra series has been used for modeling the memory effects of non-linear systems [35], [36], but this approach simplifies the measurements required to extract a valid model for the RF passband. The proposed approach is to use the Volterra Series to be able to accurately model these nonlinearities so that designers can see how to mitigate the nonlinear effects.

5.1 Introduction

An LNA has baseband memory effects which are up-converted to the RF signal and introduce asymmetry in the IMD3 terms. When the LNA is weakly nonlinear, these memory effects can often be modeled accurately by using a third-order Volterra series. This Volterra model can describe the memory effects and impact on the IMD3 terms with good accuracy in many cases. Since the LNA is only being operated in a weakly non-

linear state, the LNA can be sufficiently modeled with a third order series. In a two-tone test, only these third-order IMD frequencies are in the radio-frequency (RF) operating bandwidth, as second order terms result only at baseband and at the second harmonic frequencies. This means that the third-order frequencies are the frequencies which will cause the bandwidth near the RF signal to expand through distortion. The third-order Volterra kernels can be measured for a given a bandwidth to model the non-linearity and create a simulation tool in ADS.

5.2 Simulation of Baseband Memory Effects

The baseband memory effects of an LNA are visible in ADS two-tone simulations. It has been shown by Remley [37] that asymmetry in the third order intermodulation distortion terms (IMD3) stems from baseband memory effects that are up-converted into the RF band. The asymmetry is present because the gain modulation occurs at the envelope frequency of the two tones instead of the two excitation tones. These IMD3 terms can be seen in two tone simulations in ADS to be a function of the tone spacing and the DC bias circuit of the DUT. Simulations in ADS were run to examine the effects of tone spacing and DC bias circuitry on the IMD3 tones. If the tones became asymmetrical in magnitude, then the baseband memory effects would be shown to be present. The ADS schematic used in a Harmonic Balance simulation is shown below and was based on the ADS design guide example for a two-tone test.

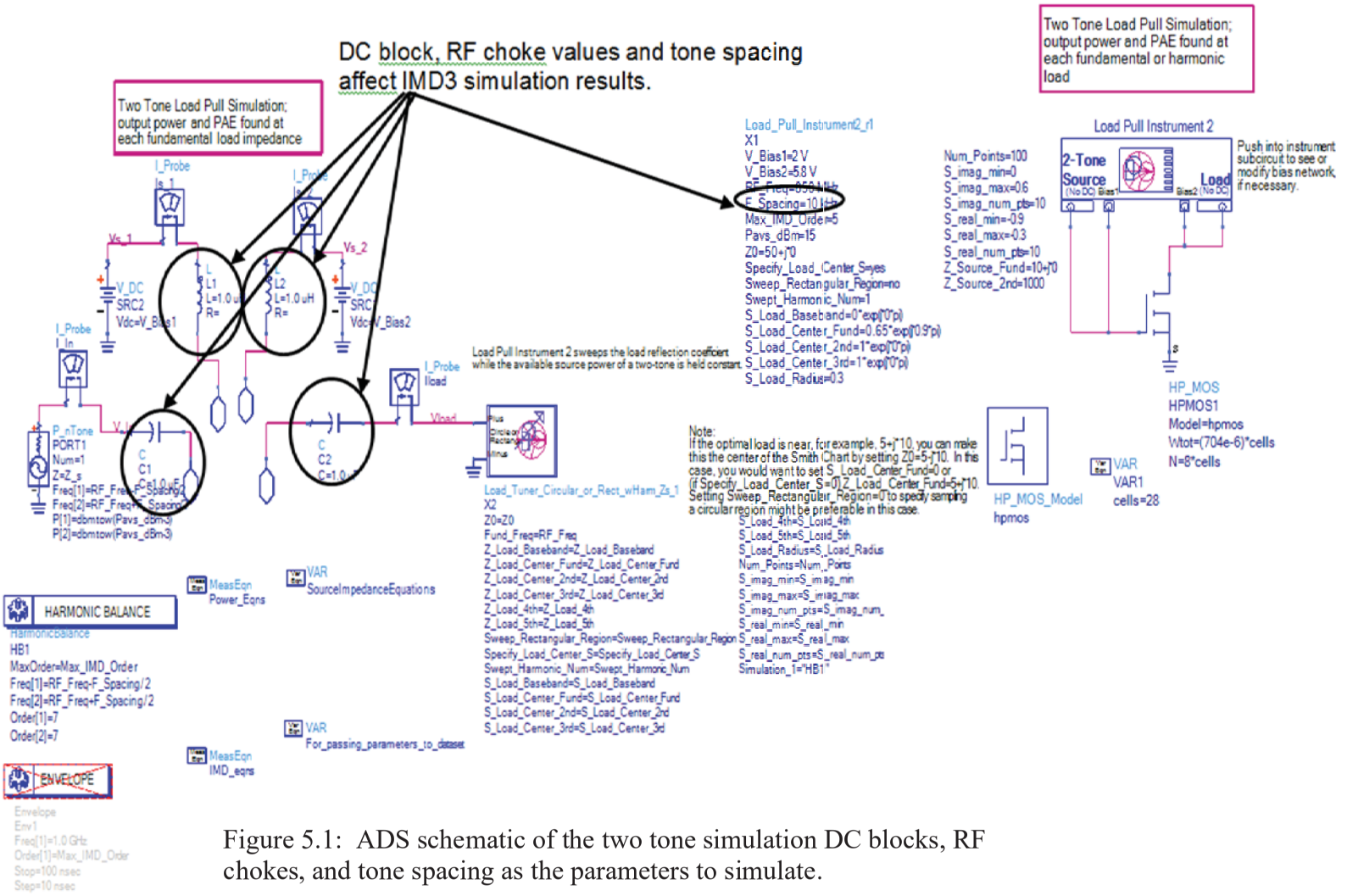

Figure 5.1: ADS schematic of the two tone simulation DC blocks, RF chokes, and tone spacing as the parameters to simulate.

The inductance and capacitance of the RF chokes and DC blocks were varied in simulation to see the IMD3 tones responded. Dr. Charles Baylis performed these simulations, and the results are shown in Figure 5.2 and Figure 5.3 below.

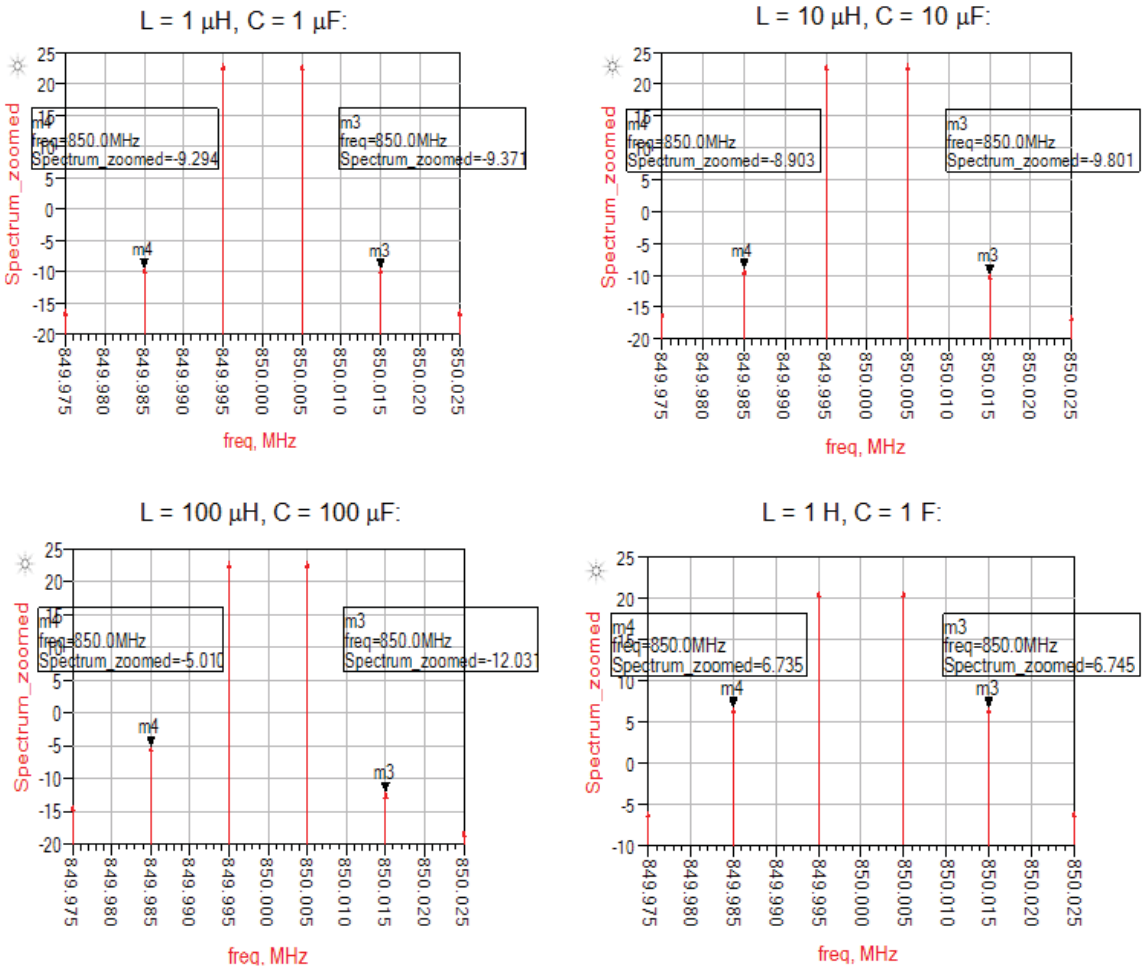

Figure 5.2: IMD3 products are higher for higher L, C. The IMD3 terms are asymmetric in transition range of L and C.

The IMD3 products are clearly seen to be a function of L and C in Figure 5.2 at the marker 3 and marker 4. They become asymmetric at L = 100µH and C = 100µF. Further simulation demonstrated that the asymmetry is mostly due to the inductance. Figure 5.3 shows the dependence of the IMD3 terms on the inductance of the RF chokes.

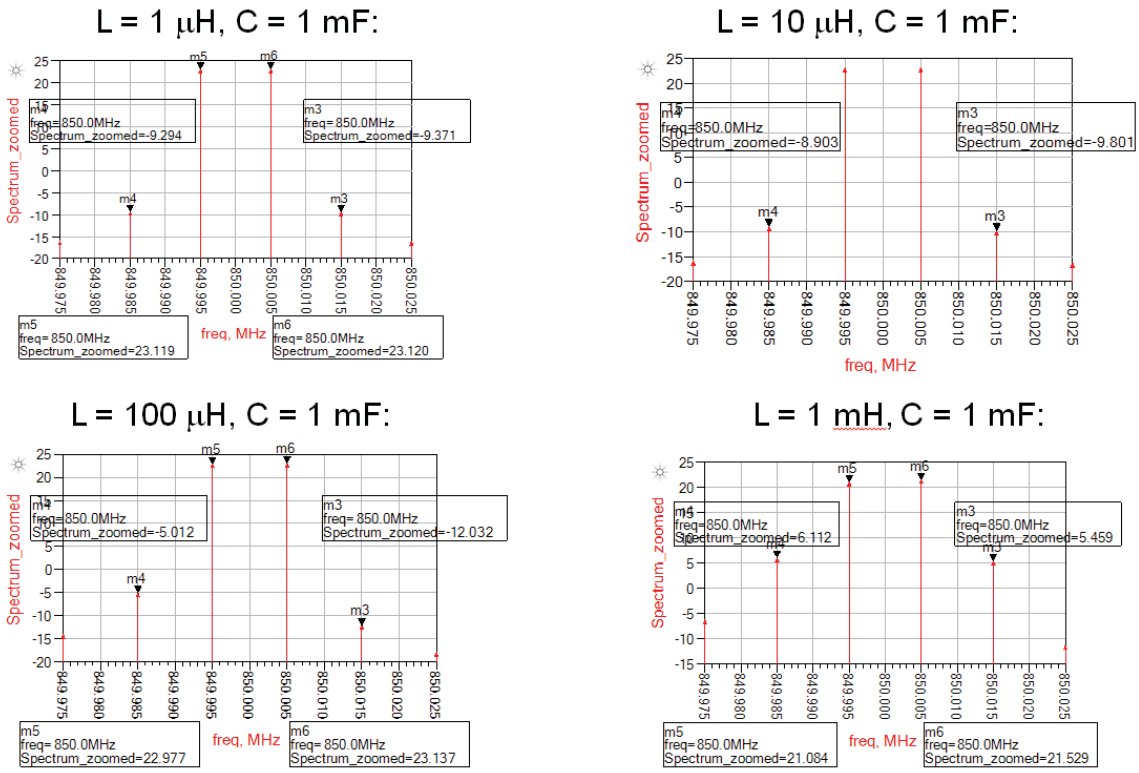

Figure 5.3: The inductance of the RF choke appears to be the dominant factor in the IMD3 products.

In Figure 5.3, the DC block capacitors were held constant and the inductance of the RF chokes were varied. For low L, the envelope frequency is passed by the inductors to the DC supply (AC ground). For high L, the envelope frequency is blocked resulting in higher IMD3 products.

The tone spacing was also varied in ADS simulation to determine its effect on the IMD3 tones. The difference frequency of the two tones is a baseband frequency which will change based upon the tone spacing. The same ADS schematic was used as shown above in Figure 5.1, and the results are shown below.

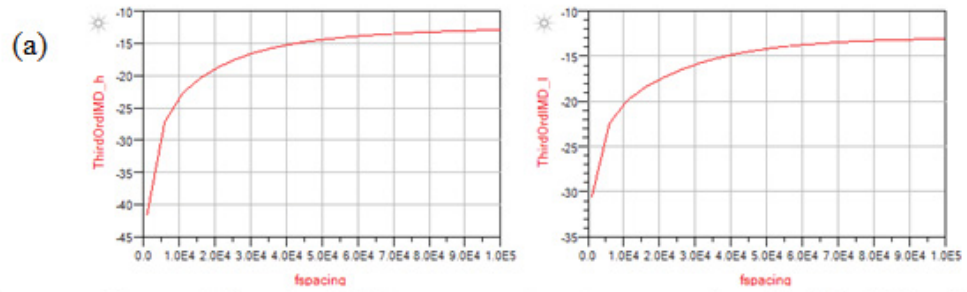

Upper and lower 3rd order IMD terms vs. two-tone spacing (1-100 kHz) with an RF choke inductor at L = 1mH and a DC block capacitor at C = 1 μH.

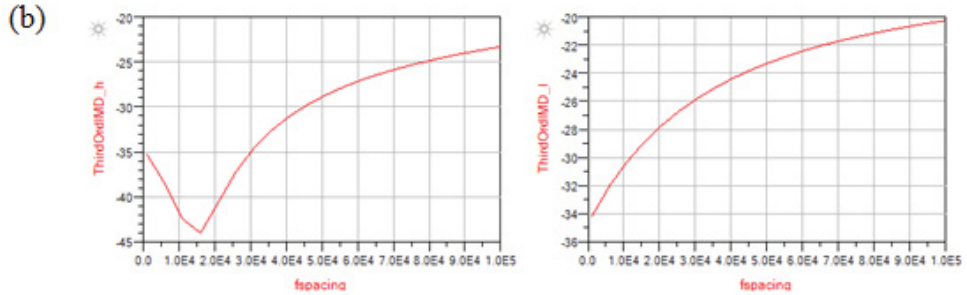

Upper and lower 3rd order IMD terms vs. two tone spacing (1-100 kHz) with an RF choke inductor at L = 0.1mH and a DC block capacitor at C = 0.1 μH.

Figure 5.4: IMD3 products as a function of tone spacing.

In Figure 5.4, the higher inductance value in (a) has symmetry in the upper and lower IMD3 products. In case (b), there is significant asymmetry in the IMD3 products. This is a result of the frequency-dependence of the bias network. The upper and lower IMD3 terms are further apart for larger tone spacing and therefore the asymmetry is more pronounced.

5.3 Volterra Series

The Volterra Series is a powerful tool which can enable better modeling of memory effects in a system. The Volterra Series combines ideas from the Taylor Series and Linear Time Invariant (LTI) systems. The Volterra Series can be seen as a

generalization of the Taylor Series that provides memory effects [38]. The Taylor Series for a function y is

$$\begin{aligned} y(t) &= \sum_{n=0}^{\infty} \alpha_n x^n(t) \\ &= \alpha_0 + \alpha_1 x(t) + \alpha_2 x^2(t) + \alpha_3 x^3(t) + \cdots . \end{aligned} \tag{5.1}$$

To see the similarity, the Volterra Series for a function is shown as

$$\begin{aligned} y(t) = h_0(t) &+ \int_{\tau_1} x(t-\tau_1) h_1(\tau_1) d\tau_1 \\ &+ \int_{\tau_1} \int_{\tau_2} x(t-\tau_1) x(t-\tau_2) h_2(\tau_1, \tau_2) d\tau_1 d\tau_2 \\ &+ \int_{\tau_1} \int_{\tau_2} \int_{\tau_3} x(t-\tau_1) x(t-\tau_2) x(t-\tau_3) h_3(\tau_1, \tau_2, \tau_3) d\tau_1 d\tau_2 d\tau_3 + \cdots \end{aligned} \tag{5.2}$$

The functions $h_n(t_n)$ are Volterra kernels. If the system is passive, $h_0(t) = 0$. An amplifier is a passive system as there is no output when there is no input. Note that the functions $h_n(\tau)$ are n dimensional functions. Volterra kernels are similar to the impulse response, $h(t)$, of an LTI system. Each kernel represents the contribution to the output of its order. The $h_1(t_1)$ is the first order response, $h_2(t_1, t_2)$ is the second order response, and so on. For our weakly non-linear amplifier, we are assuming a third order system. This means we only need to characterize our amplifier up to $h_3(t_1, t_2, t_3)$ to completely characterize the device.

5.4 Fourier Transforms of Volterra Kernels

A common technique when dealing with a Volterra series is to take the Fourier transform of the Volterra kernels to convert the Volterra kernels from the time domain to the frequency domain [39]. The Fourier transform is described by

$$H_n(u_1, u_2, \cdots, u_n) = \int_{t_1}\int_{t_2}\cdots\int_{t_n} h_n(t_1, t_2, \cdots, t_n) \times e^{-j2\pi(u_1 t_1 + u_2 t_2 + \cdots + u_n t_n} dt_1 dt_2, \cdots dt_n. \tag{5.3}$$

The frequency domain representation of the Volterra kernels allows a more intuitive understanding of the Volterra kernels as $H_1(v)$ corresponds to the amplitude at the frequency $u = v$.

5.5 Averaged Volterra Kernels

The idea of averaged Volterra kernels must be addressed to understand the measurement technique proposed later in this work. The idea of an averaged kernel can be seen in an example of a second order term. The second order terms of a Volterra model are shown as

$$y_2(t) = h_2(t-T_1, t-T_1)+h_2(t-T_1, t-T_2)+h_2(t-T_2, t-T_1)+h_2(t-T_2, t-T_2). \tag{5.4}$$

The two middle terms can be combined to get an averaged kernel where

$$\hat{h}(t_1, t_2) = \frac{1}{2}\Big(h(t_1, t_2) + h(t_2, t_1) \Big) \tag{5.5}$$

The averaged kernel is symmetric and so (5.4) can be rewritten as

$$y_2(t) = h_2(t - T_1, t - T_1) + 2\hat{h}_2(t - T_1, t - T_2) + h_2(t - T_2, t - T_2). \tag{5.6}$$

The nth order kernel, $h_n(t_1, t_2, t_3, \ldots, t_n)$ will have $n!$ distinct permutations. Therefore the nth order averaged kernel, $\hat{h}_n(t_1, t_2, t_3, \ldots, t_n) = \frac{1}{n!} h_n(t_1, t_2, t_3, \ldots, t_n)$.

5.6 Volterra Model for a Two Tone Input to a 3rd Order Model

For a two tone input to a third order system, Figure 5.5 shows the output spectrum as described by the Volterra kernels.

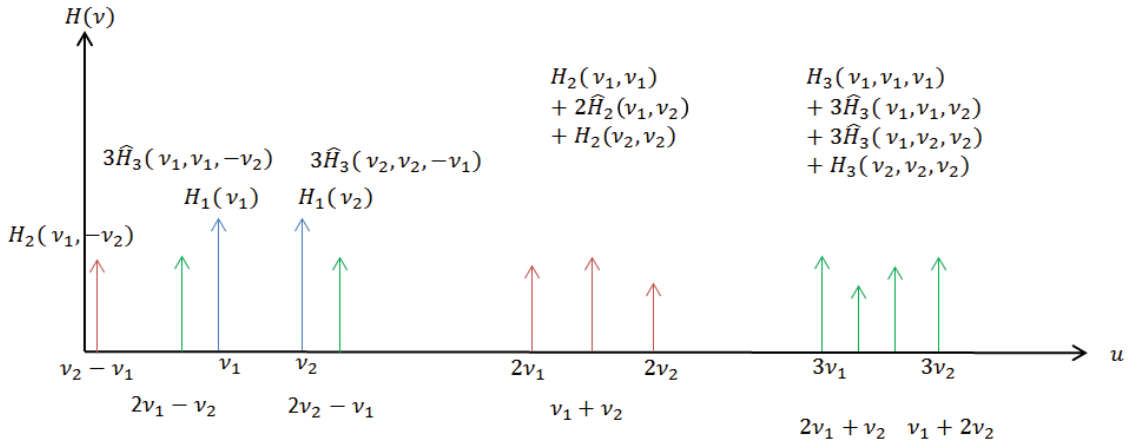

Figure 5.5: Constructing the output frequency terms for two sinusoids, ν_1 and ν_2, stimulating a third order system.

For a two tone input, a third order system will have 12 tones on the output. If these tones are all measured for a range of two tone inputs, the full Volterra kernel can be extracted to make a model of the system. The size of the Volterra kernels for even a small range of two tone inputs will quickly grow too large to be manageable and measureable. However, the above figure shows that in a third order system, there are no second order terms in the RF passband. The only terms present in the RF passband are from the $\widehat{H}_3(\nu_1,\nu_1,-\nu_2)$ and $\widehat{H}_3(\nu_2,\nu_2,-\nu_1)$ terms in the Volterra kernel. This is illustrated in Figure 5.6, which shows frequencies near the passband for a two-tone input. Only odd order terms will be present in the passband of the RF band.

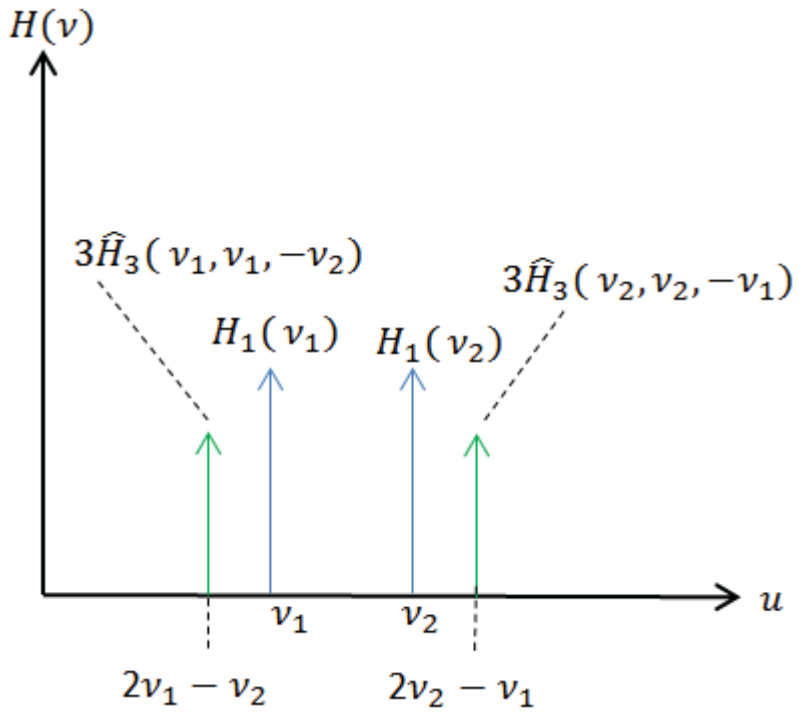

Figure 5.6: Zoomed in RF passband of Figure 5.5. Only terms present in the passband beside the two input tones are the third order terms at $u = 2\nu_1 - \nu_2$ and $u = 2\nu_2 - \nu_1$.

These averaged Volterra kernels components $\hat{H}_3(\nu_1, \nu_1, -\nu_2)$ and $\hat{H}_3(\nu_2, \nu_2, -\nu_1)$ occur at the IMD3 frequencies as simulated in ADS shown in Figures 5.2, 5.3, and 5.4. By measuring the averaged third-order Volterra kernels of a system from a multi-tone input, the RF passband of the system can be modelled to understand the linearity in the passband. By ignoring the entire second-order kernel and the third order terms which will occur outside the passband, the size of the Volterra model will be significantly reduced. This size reduction will allow for easier model extraction and for faster simulation of the model.

5.7 Three-Tone Volterra Model

For an nth order Volterra kernel, $H_3(\nu_1, \nu_2, \ldots, -\nu_n)$, it has been shown that n number sinusoids must be input to fully measure the Volterra kernel. To extract a complete model for a third order system, three sinusoids must be swept through all combinations of frequencies in the model's bandwidth to extract each contribution of each Volterra term. For a large characterized model bandwidth, the size of the third order Volterra kernel will be extremely large, even when only considering the in-band terms. The process to completely characterize a third order system for a given bandwidth is shown in the following figure.

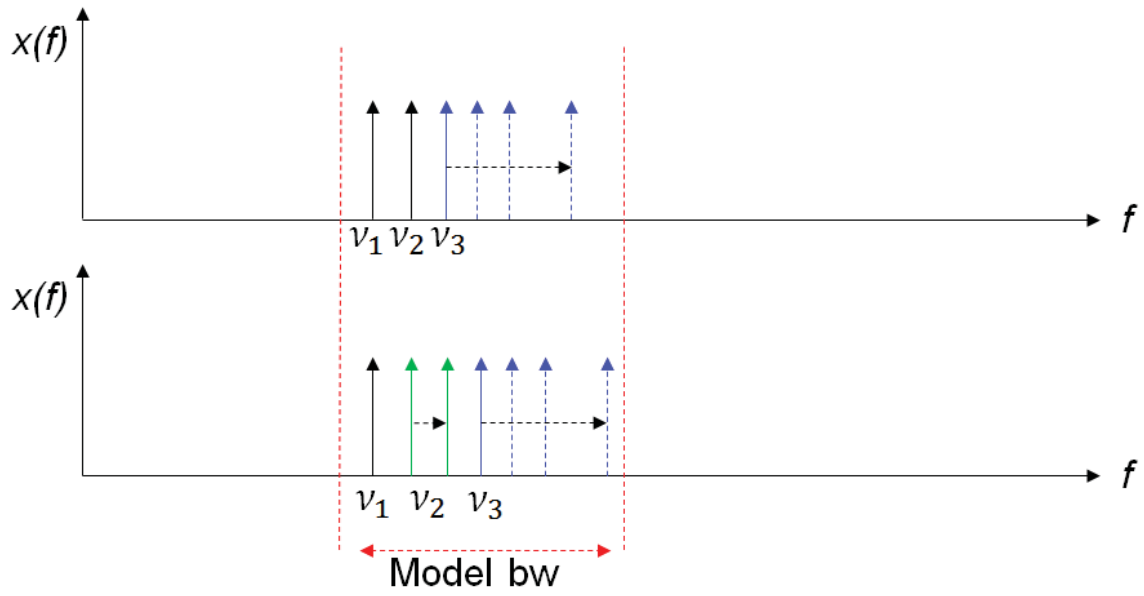

Figure 5.7: Using three tones to extract the full Volterra model for the bandwidth. Measurements must be made at each combination of ν_1, ν_2, ν_3.

5.8 Two-Tone Volterra Approximation of Three-Tone Model

Sweeping three tones through every combination of frequencies in a bandwidth will require a very large number of measurements. Also, most RF measurement

equipment is capable of producing two tones for standard bench measurements, such as a third-order intercept test. The ability to approximate a third order system by sweeping two tones instead of three tones will allow for fewer measurements and a simpler measurement setup.

A two tone approximation of three tones can be more easily visualized by approximating two tones with one tone as seen in Figure 5.8.

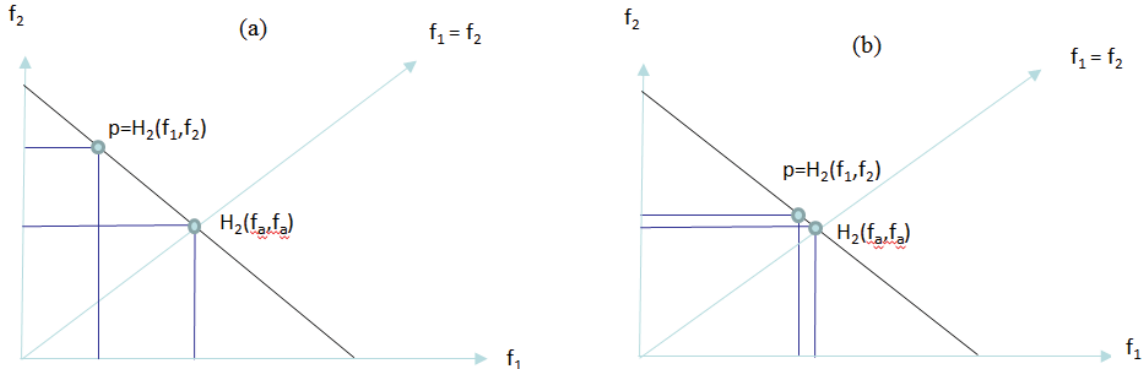

Figure 5.8: The approximation of p by $H_2(f_a, f_a)$ gets better as f_1 approaches f_2 where $f_a = \frac{(f_1+f_2)}{2}$.

Figure 5.8 shows a point in two-dimensions, $H_2(f_1, f_2)$, can be approximated by the average, $H_2(f_a, f_a)$ which falls upon the $f_1 = f_2$ line. The closer the two tones are in frequency, the better the approximation will be by the one average tone as seen in Figure 5.8(b). If a maximum error limit is set for how far away a point can be from the $f_1 = f_2$ line, then a two-dimensional channel along that line can be modeled by the one-dimensional line going through the search space. This idea is illustrated in Figure 5.9.

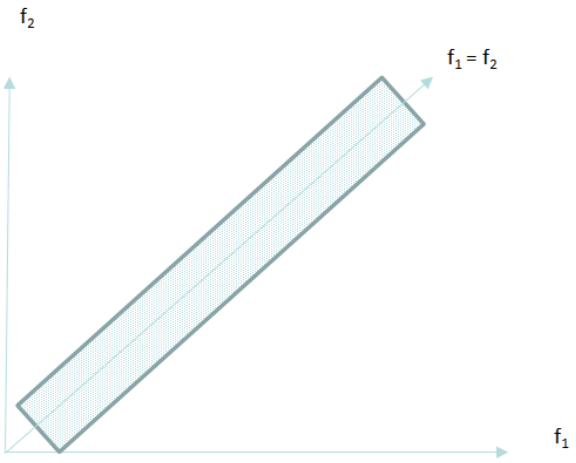

Figure 5.9: Channel where approximation of $H_2(f_1, f_2)$ by $H_2(f_a, f_a)$ is valid.

Figure 5.9 shows that the Volterra kernel, $H_2(f_a, f_a)$, is still a second order effect, but it can be measured by using only the one average tone. The approximation is valid for a small 2D rectangle around the $f_1 = f_2$ line in the 2D space.

This same principle can be applied to a two-tone approximation of a three-tone measurement. A third order effect, $H_3(f_1, f_2, -f_3)$, can be approximated by $H_3(f_a, f_a, -f_3)$. For a two-tone approximation of three tones, the first two tones, f_1 and f_2, can be approximated by f_a. The second tone will be at f_3. Similar to the one-tone approximation show in Figure 5.9, the two-tone approximation will be valid for a small rectangular volume around the $f_1 = f_2$ plane in the 3D space. A third order effect due to a combination of three tones in the passband can be approximated with a combination of two tones. Figure 5.10 shows an example.

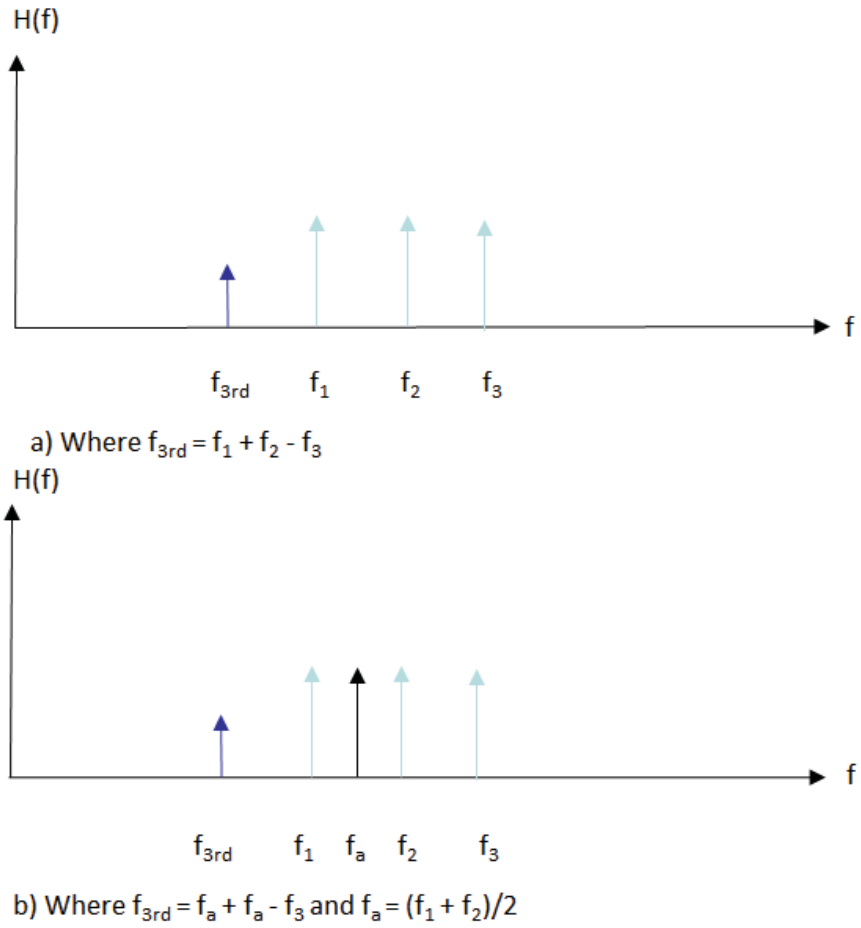

Figure 5.10: (a) Modeling the third order term, f_{3rd}, by $H_3(f_1, f_2, -f_3)$.
(b) Modeling the third order term, f_{3rd}, by $H_3(f_a, f_a, -f_3)$.

The third order effect is seen in both (a) and (b) at the frequency, f_{3rd}. If f_1 and f_2 are close, the error introduced by the approximation will be small. Since f_1, f_2, and f_a are in the RF passband, the distance between them is relatively small.

5.9 Proposed Measurement Verification

The next step of this research is to verify this proposed method of using two tones to approximate the third order Volterra kernel on a measurement test bench with an LNA. The outline of the planned measurement setup is straightforward. The planned setup will use a Keysight Technologies PNA-X, two comb generators, a splitter, a computer with

MATLAB to automate the measurements, six SMA cables, two bias tees, and a MWT-173 FET as the device to test. The test will use a center frequency of 1.3GHz and will characterize a bandwidth of 200KHz as a starting point. The two tones can be swept through at a spacing of 10KHz. MATLAB can be used to automate the sweeping of the two tones and the data acquisition for integration into a device model. Figure 5.11 shows the proposed measurement setup.

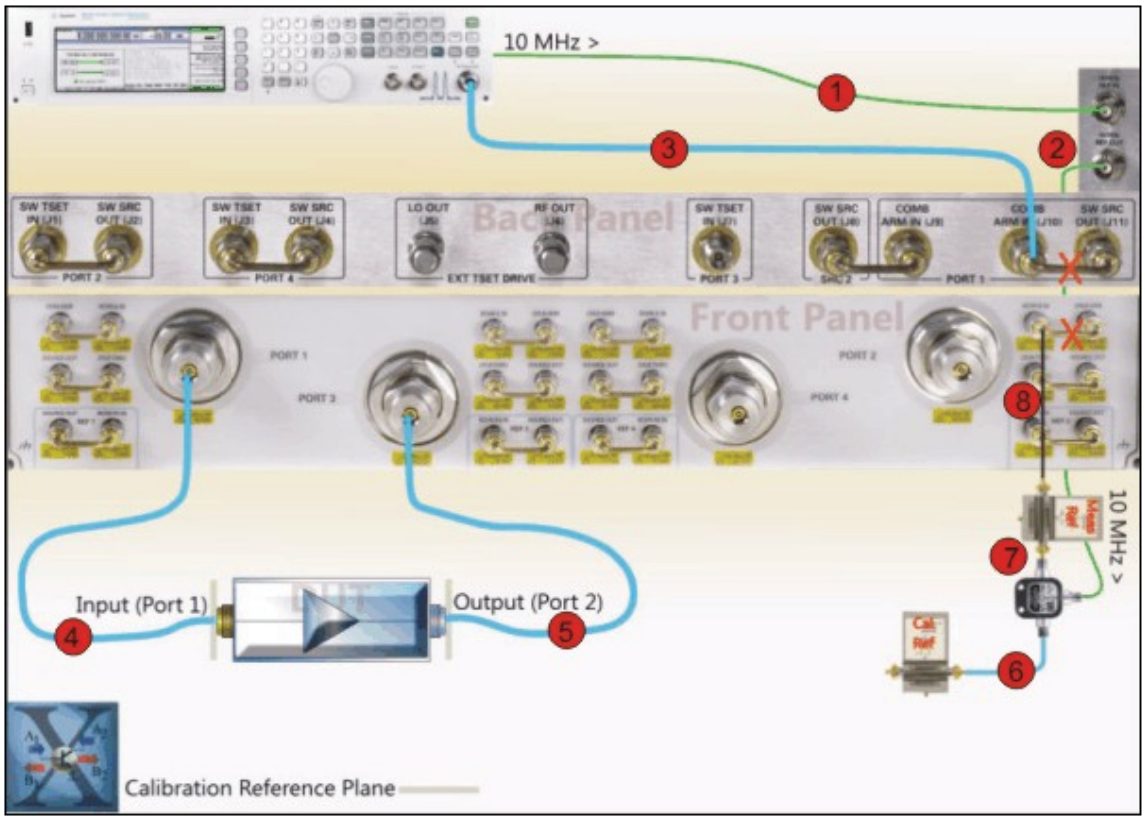

Figure 5.11: Proposed Measurement Setup for Two-Tone Measurement.

Figure 5.11 shows that PNA-X connected to the device and synced with the signal generator. The one comb generator will provide the calibration and the other comb generator will provide the reference phase for the IMD3 terms.

To calibrate the PNA to measure at the correct reference plane, both the magnitude and phase must be considered. The magnitude calibration can be done using the standard SOLT calibration technique. Measuring the phase of a third order term is just as important as the magnitude for a Volterra characterization. However, for a two tone input to a system, f_1 and f_2, there is no input at a third order term frequency such as $2f_1 - f_2$ to allow for a reference phase to be determined at the output at the third order frequency. The comb generator must be used to generate a constant reference phase at the frequencies $2f_1 - f_2$ and $2f_2 - f_1$ to allow meaningful phase information to be obtained from the output of the device. This technique has been demonstrated in [40] to obtain a valid phase calibration.

Once the PNA is calibrated to the device's output plane, MATLAB can begin iteratively measuring the magnitude and phase of the output of the device at each combination of the two tones throughout the bandwidth to be characterized. At each frequency combination, (f_1, f_2), the value for $3\widehat{H}_3(\nu_1, \nu_1, -\nu_2)$ and $3\widehat{H}_3(\nu_2, \nu_2, -\nu_1)$ can be determined. The results can be formed into a matrix of for all values of $\widehat{H}_3(\nu_1, \nu_1, -\nu_2)$. A Volterra device model can be created from this matrix. The model would be able to simulate the output of the device in the RF passband by looking up the best values of $\widehat{H}_3(\nu_a, \nu_a, -\nu_3)$ for any third order term, $\widehat{H}_3(\nu_1, \nu_2, -\nu_3)$. The model could then be tested by comparing the model's output predictions for a given input and the output of the device on the bench for that same given input. Figure 5.11 illustrates the proposed test setup.

5.10 Summary of the Volterra Model

The two-tone Volterra characterization of a third order system can be made into a model which can accurately simulate baseband memory effects. Baseband memory degrades the linearity of the RF passband of LNAs. Better modeling and simulation can help improve the design of LNAs to remove the baseband memory effects and achieve higher linearity. The Volterra series is an excellent tool for modeling memory effects. The approximation of the third order kernel with two tones greatly reduces the size of the Volterra model and the number of measurements required to extract the model. The proposed measurements would verify that the Volterra model was able to successfully simulate these memory effects and give confidence in using the model for LNA design.

CHAPTER SIX

Conclusions

This thesis has detailed two areas of innovation for next-generation radar systems. First, reconfiguration of tunable circuitry for radar transmitter applications was demonstrated with two different circuit types. Secondly, a method for extraction of a Volterra model from a two tone measurement has been discussed, which is expected to allow more accurate simulation of the in-band nonlinearity products of low-noise amplifiers (LNAs) in weakly nonlinear mode.

For the circuitry optimizations, the strengths and weaknesses of each tuner were determined through experimentation, and the optimization algorithms were developed to compliment the strengths and mitigate the weaknesses of each device. A search algorithm was demonstrated using direct tuning of varactor bias voltages in a varactor matching network. Despite the multimodality of the contours in the varactor bias-voltage space, the gradient search was still able to find the constrained PAE/ACPR optimum operating point. Direct tuning using the cavity position numbers of a high-power evanescent-mode cavity tuner was also demonstrated. This eliminates the need for a time-consuming and unreliable characterization before the optimization as well as table lookups during the optimization, saving time in each measurement. This tuner can handle the higher RF power levels, while still being quickly reconfigurable.

The method for extracting a third-order Volterra model for a weakly nonlinear device will help designers improve the linearity of radar receivers. The two-tone

approximation for the three-tone measurement reduces the complexity of the measurement setup as well as saving a significant number of measurements to extract a valid Volterra characterization of the third-order terms. Baseband memory effects, which are up-converted to the RF bandwidth of the signal, will be more accurately simulated with this model, and designers can use these simulations to mitigate the effects to the LNA.

In ongoing and future work, the circuit optimizations will switch from using ACPR to a spectral mask to measure the spectral compliance of the transmitted signal. A spectral mask is the metric used by the FCC to determine if a device is in spectral compliance. Both metrics give similar results for keeping the transmitted signal from interfering with neighboring channels. A spectral mask determines the maximum power the device can transmit at any frequency while the ACPR only looks at only specific side bands defined by the user. These algorithms will also be implemented into a real radar system to determine how the optimization techniques perform with an actual radar system on the bench. The Volterra model for third-order systems needs to be verified in measurement using the steps outlined in this thesis. The extraction of the third-order Volterra kernel and simulation of a device will need to be compared to measurement results of a device to determine whether the memory effects are properly modeled by the Volterra series behavior model.

The optimization techniques for the radar transmitter and the modeling technique presented for a receiver improve on the current state of radar system design. Reconfigurable circuitry will allow for the cognitive radar systems to operate efficiently, and the accurate modeling of memory effects of LNAs ensures higher effectiveness of

radar receivers. The search algorithms and the new Volterra modeling method can contribute to the success of future radar systems.

BIBLIOGRAPHY

[1] Guerci, Joseph R. "Cognitive radar: a knowledge-aided fully adaptive approach." *Radar Conference, 2010 IEEE*. IEEE, 2010.

[2] L. Lamers *et al*., "Comparison of bias-voltage and reflection-coefficient based reconfiguration of a tunable-varactor matching network for adaptive amplifiers," *2017 IEEE 18th Wireless and Microwave Technology Conference (WAMICON)*, Cocoa Beach, FL, 2017, pp. 1-5.

[3] Z. Hays *et al*., "Fast amplifier PAE optimization using resonant frequency interval halving with an evanescent-mode cavity tuner," *2017 Texas Symposium on Wireless and Microwave Circuits and Systems (WMCS)*, Waco, TX, 2017, pp. 1-3.

[4] C. Baylis *et al*., "Designing transmitters for spectral conformity: power amplifier design issues and strategies," in *IET Radar, Sonar & Navigation*, vol. 5, no. 6, pp. 681-685, July 2011.

[5] F. Raab, P. Asbeck, S. Cripps, P. Kenington, Z. Popovic, N. Pothecary, J. Sevic, and N. Sokal, “RF and Microwave Power Amplifier and Transmitter Topologies, Part 1,” *High Frequency Electronics*, May 2003.

[6] J. Martin, *Adaptive Load Impedance Optimization for Power Amplifiers in Reconfigurable Radar Transmitters*, Master’s Thesis, Baylor University, 2012.

[7] Y. Collette and P. Siarry, *Multiobjective Optimization: Principles and Case Studies*, Springer, 2004.

[8] C. Baylis, L. Dunleavy, S. Lardizabal, R.J. Marks II, and A. Rodriguez, “Efficient Optimization Using Experimental Queries: A Peak-Search Algorithm for Efficient Load-Pull Measurements,” *Journal of Advanced Computational Intelligence and Intelligent Informatics*, Vol. 15, No. 1, January 2011.

[9] M. Fellows, C. Baylis, J. Martin, L. Cohen and R. J. Marks, "Direct algorithm for the Pareto load-pull optimisation of power-added efficiency and adjacent-channel power ratio," in *IET Radar, Sonar & Navigation*, vol. 8, no. 9, pp. 1280-1287, 12 2014.

[10] M. Fellows, L. Lamers, C. Baylis, L. Cohen and R. J. Marks, "A fast load-pull optimization for power-added efficiency under output power and ACPR constraints," in*IEEE Transactions on Aerospace and Electronic Systems*, vol. 52, no. 6, pp. 2906-2916, December 2016.

[11] J. Barkate *et al*., "Fast, simultaneous optimization of power amplifier input power and load impedance for power-added efficiency and adjacent-channel power ratio using the power smith tube," in *IEEE Transactions on Aerospace and Electronic Systems*, vol. 52, no. 2, pp. 928-937, April 2016.

[12] M. Fellows *et al*., "The bias smith tube: Simultaneous optimization of bias voltage and load impedance in power amplifier design," *2016 IEEE Radio and Wireless Symposium (RWS)*, Austin, TX, 2016, pp. 215-218.

[13] F. Yazdani and R. R. Mansour, "Realizing reconfigurable stub impedance matching networks using MEMS switches," *2017 47th European Microwave Conference (EuMC)*, Nuremberg, 2017, pp. 1081-1184.

[14] R. G. Pesel, S. S. Attar and R. R. Mansour, "MEMS-based switched-capacitor banks for impedance matching networks," *2015 European Microwave Conference (EuMC)*, Paris, 2015, pp. 1018-1021.

[15] V. Silva Cortes and G. Fischer, "Shunt MEMS switch requirements for Tunable Matching Network at 1.9 GHz in composite substrates," *2015 German Microwave Conference*, Nuremberg, 2015, pp. 422-425.

[16] H.M. Nemati et al., "Design of Varactor-Based Tunable Matching Networks for Dynamic Load Modulation of High Power Amplifiers", *IEEE Transactions on Microwave Theory and Techniques*, vol. 57, no. 5, pp. 1110-1118, May 2009.

[17] D. Qiao et al., "An Intelligently Controlled RF Power Amplifier with a Reconfigrable MEMS-Varactor Tuner",*IEEE Transactions on Microwave Theory and Techniques*, vol. 53, no. 3, pp. 1089-1095, March 2005.

[18] W. du Plessis, P. Abrie, "Lumped Impedance Matching Using a Hybrid Genetic Algorithm", *Microwave and Optical Technology Letters*, vol. 37, no. 3, pp. 210-212, May 2003.

[19] R. H. Flake, "Volterra series representation of nonlinear systems," in *Transactions of the American Institute of Electrical Engineers, Part II: Applications and Industry*, vol. 81, no. 6, pp. 330-335, Jan. 1963.

[20] P. Venkatappareddy and B. Lall, "Linear in the parameter model for Homomorphic filter: Volterra series based approach," *2016 11th International Conference on Industrial and Information Systems (ICIIS)*, Roorkee, India, 2016, pp. 650-654.

[21] S. Serunjogi, M. A. Sanduleanu and M. S. Rasras, "Volterra Series Based Linearity Analysis of a Phase Modulated Microwave Photonic Link," in *Journal of Lightwave Technology*, vol. PP, no. 99, pp. 1-1.

[22] R. N. Braithwaite, "Digital Predistortion of an RF Power Amplifier Using a Reduced Volterra Series Model With a Memory Polynomial Estimator," in *IEEE Transactions on Microwave Theory and Techniques*, vol. 65, no. 10, pp. 3613-3623, Oct. 2017.

[23] H. Zhao, J. Wang and X. Li, "Modeling of low noise amplifier based on volterra series with recursive least square algorithm," *2017 International Applied Computational Electromagnetics Society Symposium (ACES)*, Suzhou, 2017, pp. 1-2.

[24] H. Yu, K. El-Sankary and E. I. El-Masry, "Distortion Analysis Using Volterra Series and Linearization Technique of Nano-Scale Bulk-Driven CMOS RF Amplifier," in*IEEE Transactions on Circuits and Systems I: Regular Papers*, vol. 62, no. 1, pp. 19-28, Jan. 2015.

[25] D. D. Silveira, L. S. Araujo, T. V. N. Coelho and A. B. dos Santos, "Considerations about the number of coefficients used in Volterra series models for RF Power Amplifiers," *2015 SBMO/IEEE MTT-S International Microwave and Optoelectronics Conference (IMOC)*, Porto de Galinhas, 2015, pp. 1-4.

[26] R. N. Braithwaite, "Pruning strategies for a Volterra series model used in digital predistortion (DPD) of RF power amplifiers," *2017 IEEE Topical Conference on RF/Microwave Power Amplifiers for Radio and Wireless Applications (PAWR)*, Phoenix, AZ, 2017, pp. 4-7.

[27] S. Boyd, Y. Tang and L. Chua, "Measuring Volterra kernels," in *IEEE Transactions on Circuits and Systems*, vol. 30, no. 8, pp. 571-577, Aug 1983.

[28] N. Bjorsell, P. Suchanek, P. Handel and D. Ronnow, "Measuring Volterra Kernels of Analog-to-Digital Converters Using a Stepped Three-Tone Scan," in *IEEE Transactions on Instrumentation and Measurement*, vol. 57, no. 4, pp. 666-671, April 2008.

[29] S. Kumar and S. Kumari, "Design of low power, high gain LNA for WCDMA range and parameters extraction using Artificial Neural Network (ANN)," *2015 IEEE Power, Communication and Information Technology Conference (PCITC)*, Bhubaneswar, 2015, pp. 436-441.

[30] A. Nieuwoudt, T. Ragheb, H. Nejati and Y. Massoud, "Numerical Design Optimization Methodology for Wideband and Multi-Band Inductively Degenerated Cascode CMOS Low Noise Amplifiers," in *IEEE Transactions on Circuits and Systems I: Regular Papers*, vol. 56, no. 6, pp. 1088-1101, June 2009.

[31] V. Rizzoli, D. Masotti, F. Mastri and E. Montanari, "System-Oriented Harmonic-Balance Algorithms for Circuit-Level Simulation," in *IEEE Transactions on Computer-Aided Design of Integrated Circuits and Systems*, vol. 30, no. 2, pp. 256-269, Feb. 2011.

[32] Z. Hays *et al*., "Real-time amplifier optimization algorithm for adaptive radio using a tunable-varactor matching network," *2017 IEEE Radio and Wireless Symposium (RWS)*, Phoenix, AZ, 2017, pp. 215-217.

[33] Y. C. Wu, M. Abu Khater, A. Semnani and D. Peroulis, "An S-band 3-W load-reconfigurable power amplifier with 50–76% efficiency for VSWR up to 4:1," *2017 IEEE MTT-S International Microwave Symposium (IMS)*, Honololu, HI, 2017, pp. 2041-2044.

[34] M. A. Chaudhary, Z. A. Memon, J. Lees, J. Benedikt and P. Tasker, "Investigation of baseband electrical memory effects on the dynamic characteristics of power transistors," INMIC, Lahore, 2013, pp. 106-109.

[35] S. K. Myoung, D. Chaillot, P. Roblin, W. Dai, S. J. Doo, “Volterra characterization and predistortion linearization of multi-carrier power ampliflers,” in Microwave Measurements Conference, 2004, p. 65-73.

[36] S. Jinlong, L. Maoliu and W. Zhilu, "Characterization of harmonic distortion and memory effects for RF power amplifiers based on volterra algorithm," 2014 XXXIth URSI General Assembly and Scientific Symposium (URSI GASS), Beijing, 2014, pp. 1-4.

[37] K. Remley, D. Williams, D. M. M.-P. Schreurs, and J. Wood, “Simplifying and Interpreting Two-Tone Measurements,” IEEE Transactions of Microwave Theory and Techniques, vol. 52, pp. 2576-2584, Nov. 2004.

[38] C. M. Lesiak and A. J. Krener, "The existence and uniqueness of volterra series for nonlinear systems," 1977 IEEE Conference on Decision and Control including the 16th Symposium on Adaptive Processes and A Special Symposium on Fuzzy Set Theory and Applications, New Orleans, LA, USA, 1977, pp. 271-274.

[39] S. Narayanan, "Transistor distortion analysis using volterra series representation," in The Bell System Technical Journal, vol. 46, no. 5, pp. 991-1024, May-June 1967.

[40] S. Futatsumori et al., "Precise Measurement of IMD Behavior in 5-GHz HTS Resonators and Evaluation of Nonlinear Microwave Characteristics," in IEEE Transactions on Applied Superconductivity, vol. 19, no. 3, pp. 3595-3599, June 2009.

[41] M. Fellows, C. Baylis, L. Cohen and R. J. Marks II, "Real-time load impedance optimization for radar spectral mask compliance and power efficiency," in *IEEE Transactions on Aerospace and Electronic Systems*, vol. 51, no. 1, pp. 591-599, January 2015.

[42] Z. Hays, C. Kappelmann, L. Lamers, C. Baylis, M. A. Khater, A. Semnani, D. Peroulis, E. Vivieros, J. Penn, "Fast impedance matching using interval halving of resonator position numbers for a high-power evanescent-mode cavity tuner," *2018 IEEE Radio and Wireless Symposium (RWS)*, Anaheim, CA, USA, 2018, pp. 256-258.

[43] S. Rezayet, “Circuit Optimization and Frequency Agility for Cognitive Radar,” Master’s Thesis, Baylor University, 2018.